PCCP

PAPER

View Article Online
View Journal | View Issue

Cite this: *Phys. Chem. Chem. Phys.*, 2022, **24**, 24767

Ultrafast 2D-IR spectroscopy of [NiFe] hydrogenase from *E. coli* reveals the role of the protein scaffold in controlling the active site environment†

Solomon L. D. Wrathall,‡[a] Barbara Procacci,‡[a] Marius Horch,[b] Emily Saxton,[a] Chris Furlan,[a] Julia Walton,[a] Yvonne Rippers,[b] James N. Blaza,[a] Gregory M. Greetham,[c] Michael Towrie,[c] Anthony W. Parker,[c] Jason Lynam,[a] Alison Parkin *[a] and Neil T. Hunt *[a]

Ultrafast two-dimensional infrared (2D-IR) spectroscopy of *Escherichia coli* Hyd-1 (*Ec*Hyd-1) reveals the structural and dynamic influence of the protein scaffold on the $Fe(CO)(CN)_2$ unit of the active site. Measurements on as-isolated *Ec*Hyd-1 probed a mixture of active site states including two, which we assign to Ni_r-$S_{I/II}$, that have not been previously observed in the *E. coli* enzyme. Explicit assignment of carbonyl (CO) and cyanide (CN) stretching bands to each state is enabled by 2D-IR. Energies of vibrational levels up to and including two-quantum vibrationally excited states of the CO and CN modes have been determined along with the associated vibrational relaxation dynamics. The carbonyl stretching mode potential is well described by a Morse function and couples weakly to the cyanide stretching vibrations. In contrast, the two CN stretching modes exhibit extremely strong coupling, leading to the observation of formally forbidden vibrational transitions in the 2D-IR spectra. We show that the vibrational relaxation times and structural dynamics of the CO and CN ligand stretching modes of the enzyme active site differ markedly from those of a model compound $K[CpFe(CO)(CN)_2]$ in aqueous solution and conclude that the protein scaffold creates a unique biomolecular environment for the NiFe site that cannot be represented by analogy to simple models of solvation.

Received 8th September 2022,
Accepted 29th September 2022

DOI: 10.1039/d2cp04188j

rsc.li/pccp

Introduction

The [NiFe] hydrogenases, which catalyze the interconversion of molecular hydrogen with protons and electrons ($H_2 \rightleftharpoons 2H^+ + 2e^-$) are of considerable interest in the pursuit of sustainable H_2 production technologies, because high turnover rates are achieved by an active site containing earth-abundant base metal atoms (Fig. 1).[1] Furthermore, some of the Group-1 subclass of periplasmic membrane-bound [NiFe] hydrogenases, such as Hyd-1 from *E. coli* (*Ec*Hyd-1), can sustain H_2-catalysis in the presence of O_2, leading to an 'O_2-tolerant' designation.[2] The use of hydrogenase-inspired catalysts in sustainable energy supply, and the design of synthetic systems for photo-bio H_2 production is however impeded by the lack of a complete understanding of the mechanisms of H_2 activation and evolution.[3–5]

The importance of achieving a deeper understanding of the hydrogenase active site is illustrated by the fact that, small molecules that mimic the biological reaction center have tended to be inferior H_2 evolution catalysts[5,6] indicating that the protein matrix plays an important role in controlling or defining the chemistry of the active site.[7–10] Indeed, the synthetic systems that have approached, or exceeded, enzymatic levels of performance have all featured either a significant second coordination sphere surrounding the metal centers or synthetic subsites placed within a protein matrix.[11–26] It follows that experimental techniques able to reveal the intermolecular interactions, structure and bonding of the hydrogenase active

[a] *Department of Chemistry and York Biomedical Research Institute, University of York, York, YO10 5DD, UK. E-mail: neil.hunt@york.ac.uk, alison.parkin@york.ac.uk*
[b] *Freie Universität Berlin, Department of Physics, Ultrafast Dynamics in Catalysis, Arnimallee 14, 14195 Berlin, Germany*
[c] *STFC Central Laser Facility, Research Complex at Harwell, Rutherford Appleton Laboratory, Harwell Campus, Didcot, OX11 0QX, UK*

† Electronic supplementary information (ESI) available: Details of the preparation and characterization of the enzyme samples along with supplemental figures supporting spectral assignment and analysis. See DOI: **https://doi.org/10.1039/d2cp04188j**

‡ These authors contributed equally to the work.

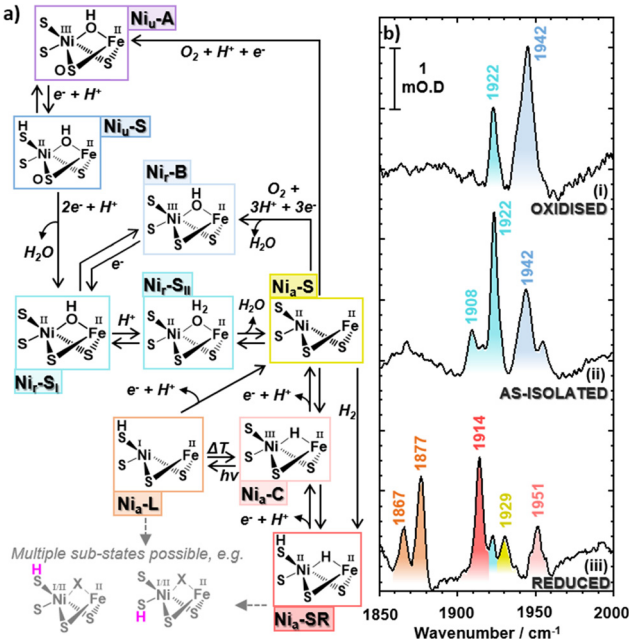

Fig. 1 (a) Catalytic cycle for *Ec*Hyd-1 with truncated structures of the bimetallic active site. (b) IR absorption (FT-IR) spectra of *Ec*Hyd-1 in the ν_{CO} region of the spectrum showing the spectrum obtained under (i) H_2-reduced and subsequently O_2 oxidized, (ii) as-isolated (aerobically purified at pH 7.6), and (iii) H_2 reduced conditions. Colored labels indicate the wavenumbers of bands due to carbonyl stretching modes and the color scheme is consistent with that in (a). The 'a' and 'r' subscripts used in state designations indicate 'active' and 'ready' active site states.

site, and quantify the modulation induced by the protein scaffold, will be valuable in determining the contributions of the second coordination sphere to H_2 generation.

The hydrogenase-catalyzed H_2 activation pathway involves a number of active site states,[1] each of which features an $Fe^{II}(CO)(CN)_2$ moiety (Fig. 1(a)). The frequencies of the stretching vibrational modes of these organometallic ligands (ν_{CO}, ν_{CN}) are sensitive to structural and redox changes of the active site. As such, IR spectroscopy has been central to the development of our current picture of hydrogenase chemistry, but a dynamic picture of the active site environment is still to fully emerge.[27–33] As hydrogen bonds to the cyanide ligands are direct of points contact between the active site and the protein scaffold, spectroscopic methods that interrogate cyanide ligand structure and dynamics will provide particularly important source of information for validating quantum chemical simulations. In turn, the conclusions obtained will enable accurate predictions with which to guide our exploitation of the hydrogenase catalytic center, ideally leading to optimized synthetic systems.

To date numerous spectroscopy tools have provided valuable data on the hydrogenases. Recently, resonance Raman spectroscopy has been used to probe metal-ligand bonding,[34–36] while nuclear resonance vibrational spectroscopy has allowed detection of bridging hydrides.[37] Advanced time resolved photogating and potential jump spectroscopies have enabled investigation of proton-coupled electron transfer processes and short-lived intermediates along the catalytic pathway.[38–45] Recently, ultrafast 2D-IR spectroscopy was used to investigate the active site of the regulatory hydrogenase from *R. eutropha* (*Re*RH). 2D-IR is an non-linear laser spectroscopy method that uses a sequence of ultrashort IR pulses to produce a two-dimensional map correlating excitation (pump) and detection (probe) frequencies.[46–51] This 2D representation of the vibrational modes of a molecule effectively places the linear IR absorption spectrum along the diagonal of the 2D-plot while off-diagonal peaks identify coupled vibrational modes.[47] The pump–probe nature of the 2D-IR experiment means that vibrational levels higher than $v = 1$ can be reached, giving information on the shape of vibrational potential energy surfaces, while pulse polarizations can be tailored to extract molecular structural information associated with mode specific orientation changes of excited modes relative to the general molecular frame. The sub-picosecond time resolution of 2D-IR means that structural and vibrational dynamics can be obtained revealing bond-specific insights into the rapid changes and interactions that occur during chemical processes.

When applied to *Re*RH, 2D-IR provided a detailed description of the ν_{CO} potential surface by accessing levels up to $v = 4$ and the associated vibrational energy relaxation mechanisms. A quantum beat phenomenon was used to identify the frequency difference between coupled vibrational modes of the two CN ligands.[52] *Re*RH has evolved to regulate the cellular production of other hydrogenases. It is purified in a single Ni(II)–Fe(II) active site state and is a relatively poor H_2-catalyst. Here, we extend our approach to study a mixture of active site states using the group 1 [NiFe] hydrogenase *Ec*Hyd-1. This enzyme enables *E. coli* to use H_2 as a fuel, with very high rates of catalytic turnover being reported (H_2-oxidation coupled to methylene blue reduction rates of approximately 65 s^{-1} at pH 6.0, and 21 ± 4 s^{-1} at pH 4.5).[53,54] We exploit the sensitivity and peak resolution of 2D-IR to probe both the ν_{CO} and ν_{CN} regions of the spectrum in detail while off-diagonal peaks enable pairs of ν_{CN} modes to be linked definitively with their ν_{CO} counterparts.[27,55] We identify the vibrational signatures of a number of states, including the Ni_r-$S_{I/II}$ active site states previously un-reported in *Ec*Hyd-1. By determining vibrational energy levels up to and including two-quantum excited states for the ν_{CO} and ν_{CN} modes as well as their vibrational and structural dynamics, we have revealed significant deviations from measurements made on the organometallic model compound K[CpFe(CO)$(CN)_2$] in solution. The results are discussed in terms of the role played by the protein scaffold in modulating the molecular environment of the active site and how 2D-IR can be employed to interrogate differences in active site states of hydrogenase enzymes to stimulate development of bio-H_2 production methods.

Experimental

Enzyme preparation and characterization

The protocol for preparation of *Ec*Hyd-1, developed from a published protocol[54] is described in the ESI.† The as-isolated enzyme was characterized using a methylene-blue H_2-oxidation

assay, protein gels, protein film electrochemistry and electron cryo-microscopy (cryo-EM). Full details of each method, including characterization data are given in the ESI† (Fig. S1–S6).

Infrared spectroscopy

For all *Ec*Hyd-1 2D-IR spectroscopy experiments, the sample (270 μM, pH 7.6) was held in a gas-tight small volume (15 μL) sandwich cell featuring CaF_2 windows and a PTFE spacer, giving an optical path length of 50 μm. For IR_{pump}–IR_{probe} and 2D-IR spectra, the samples were held at a temperature of 10 °C. For gas-cycling IR experiments, the absorption spectra were recorded at room temperature.

IR absorption spectra were recorded using a Bruker Vertex 70 spectrometer with a frequency resolution of 2 cm^{-1}. Ultrafast spectroscopy experiments were performed using the ULTRA laser system based at the UK's STFC Central Laser Facility.[56] Mid-IR pulses with a central frequency of 2000 cm^{-1}, bandwidth >300 cm^{-1}, 50 fs pulse duration and 10 kHz repetition rate were used in all cases. IR_{pump}–IR_{probe} spectra were recorded with parallel and perpendicular pump–probe polarization geometries using methods reported previously.[52] The pump–probe delay time (T_w) was scanned from −20 to 54 ps in increments of 250 fs. The spectra were acquired by frequency-dispersing the signal with a spectrograph followed by detection using 128-element Mercury–Cadmium–Telluride (MCT) array detectors, giving a frequency resolution of $\sim$2 cm^{-1}.

2D-IR spectra were acquired using the pump–probe geometry.[52] The pump pulse pair were created and the time delay between them scanned using a mid-IR pulse shaper applying a four-frame phase cycling method. 2D-IR spectra were recorded at values of T_w from 125 fs to 45 ps with parallel and perpendicular pump–probe polarization geometries. Fourier transformation of the data with respect to the time delay between the pump pulse pair was used to obtain the pump frequency axis of the 2D-IR spectrum. The probe frequency axis was generated by frequency-dispersal and detection of the signal as described for pump–probe measurements. Further details are given in the ESI.†

Results

As isolated *Ec*Hyd-1

IR absorption. The IR absorption spectrum of as-isolated *Ec*Hyd-1 in the ν_{CO} region is shown in Fig. 1(b) (panel ii). Following correction for the strongly curved baseline caused by a combination band of water located near 2100 cm^{-1} (Fig. S1(a), ESI†) three bands were identifiable in the ν_{CO} region, located at 1908, 1922 and 1942 cm^{-1}. This band pattern was found to be reproducible across multiple protein preparation processes (Fig. S2, ESI†). The corresponding ν_{CN} bands, which exhibit lower extinction coefficients than ν_{CO} bands,[58] were found to overlap significantly and so, for the purposes of state assignment, we focus here on the ν_{CO} region of the spectrum and return to the cyanide bands below.

Following previous IR absorption studies of *Ec*Hyd-1, the 1942 cm^{-1} band can be assigned to the ν_{CO} mode of the Ni_r-B state (Fig. 1(a and b), blue).[33] The band at 1922 cm^{-1} (Fig. 1(b), turquoise) appears to coincide with previous observations of the Ni_a-SR state, though the presence of such a reduced state is unexpected in an as-isolated sample.[2,57,59,60] The 1908 cm^{-1} band (Fig. 1(b), light turquoise) does not correspond to a previously reported state of *Ec*Hyd-1.

A series of additional experiments were performed to characterise the as-isolated *Ec*Hyd-1 sample in more detail and so guide the assignment of the observed ν_{CO} bands to individual active site states. Cryo-EM measurements (Fig. 2(a) and Fig. S3, ESI†) showed that the majority of enzyme molecules were present as dimers of heterodimers ($Hya(AB)_2$). This correlated with native-PAGE H_2-oxidation activity staining experiments which similarly showed that the *Ec*Hyd-1 sample had a molecular mass consistent with a dimer-of-dimers (Fig. S4, ESI†).

Further IR absorption spectroscopy experiments were performed following incubation of the as-isolated *Ec*Hyd-1 sample with 100% O_2 (Fig. 1(b), panel i). O_2 exposure resulted in an increase in intensity of the 1942 cm^{-1} band (blue) and a decrease of the 1908 and 1922 cm^{-1} bands (light turquoise). This is consistent with the assignment of the 1942 cm^{-1} band to the Ni_r-B state while the continued presence of the 1908 and 1922 cm^{-1} bands suggests that the associated states lie towards the oxidised end of the range of active site states (Fig. 1(a), blue to turquoise).[33] In contrast, reduction of the as-isolated sample by incubation with 100% H_2 (Fig. 1(b), panel iii) resulted in the loss of the 1908, 1922 and 1942 cm^{-1} bands, which were replaced by new bands at 1867 cm^{-1}, 1877 cm^{-1}, 1914 cm^{-1}, 1929 cm^{-1} and 1951 cm^{-1}. These new bands can be assigned by reference to previous work to the more reduced states of *Ec*Hyd-1: Ni_a-L_{III}, Ni_a-L_{II}, Ni_a-SR_{III}, Ni_a-S and Ni_a-C states respectively (Fig. 1(a), orange, red, yellow, pink).[33]

Given that the behavior of the 1908 and 1922 cm^{-1} bands is consistent with assignment to more oxidised active site states, we hypothesise that they can be assigned to the un-reported Ni_r-$S_{I/II}$ states. The only other candidate, the Ni_a-S state has been reported to exhibit a ν_{CO} frequency of 1929 cm^{-1} [33] while the corresponding ν_{CN} frequencies for the Ni_a-S state were in excess of 2077 cm^{-1}, which does not match our observations (*vide infra*).[33] Our assignment therefore highlights a possible coincidence of the ν_{CO} frequencies of the higher frequency Ni_r-$S_{I/II}$ state (1922 cm^{-1}) and the Ni_a-SR state,[33] though it is noted that both feature a Ni^{II} centre, which would suggest similar ν_{CO} frequencies.

To test the hypothesis that our as-isolated sample contained Ni_r-$S_{I/II}$ states rather than the more reduced Ni_a-SR state, the H_2-oxidising activities of as-isolated and H_2-activated *Ec*Hyd-1 were compared *via* methylene blue dye reduction assays (Fig. 2(c) and Fig. S5, ESI†). The activity (k_{cat}) of as-isolated *Ec*Hyd-1 samples was found to increase by almost a factor of eight (from 6.3 ± 0.2 s^{-1} to 48.7 ± 0.6 s^{-1}) following incubation with 100% H_2 (Fig. 2). This observation is consistent with the as-isolated sample shifting from oxidised to reduced active states, as expected if Ni_r-$S_{I/II}$, rather than Ni_a-SR, is present alongside Ni_r-B in the as-isolated mixture.

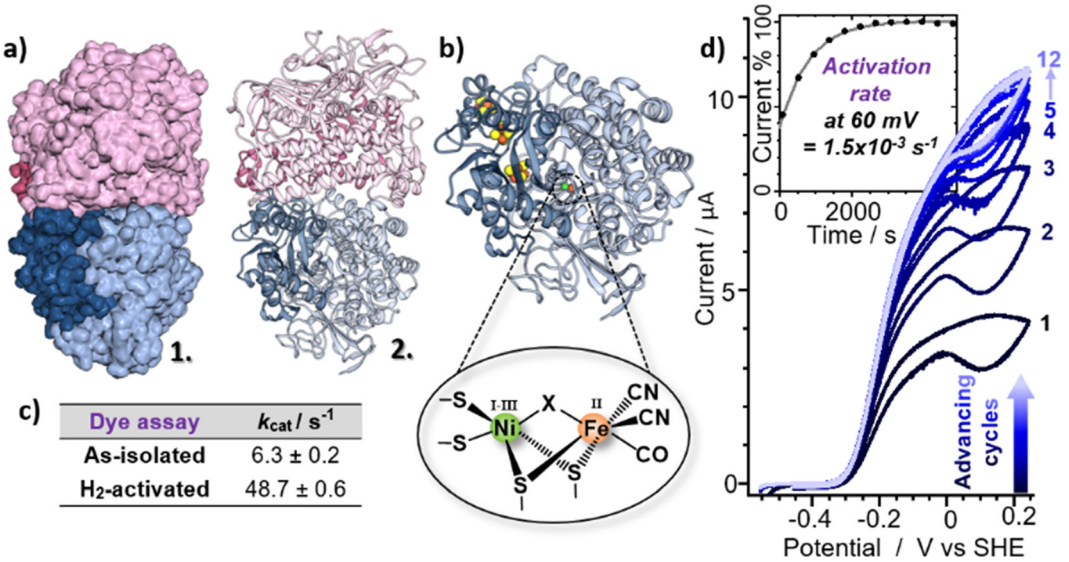

Fig. 2 (a) Model for the *Ec*Hyd-1 preparation used here based on cryo-EM 2D class images and 6FPW,[57] shown in surface mode (1) and ribbon format (2). (b) X-ray crystal structure of the monomer (PDB: 6FPW[57]) with pop-out schematic of the active site. (c) Table showing the H_2-oxidising ability of *Ec*Hyd-1 determined *via* a methylene blue dye reduction assay (three replicates). (d) Cyclic voltammograms showing the activation of *Ec*Hyd-1 with inset current/time plot showing the activation rate at 60 mV.

Protein film electrochemistry was used to monitor the activation kinetics of as-isolated *Ec*Hyd-1. Cyclic voltammetry (CV) experiments were performed in which as-isolated (*i.e.*, air-purified) *Ec*Hyd-1 was applied to the working electrode under atmospheric conditions The working electrode was then fixed into an electrochemical cell which had been pre-equilibrated with an atmosphere of 100% H_2. CV cycles were run until successive cycles resulted in no increase in positive current, indicating that all adsorbed enzyme molecules had been fully activated (Fig. 2(d) and Fig. S6, ESI†). Based on fitting the time-dependence of the change in current at 60 mV (Fig. 2(d) inset) to a monoexponential function values for $k_{activation}$ of 1.5 × 10^{-3} s^{-1} were obtained. As the obtained $k_{activation}$ value is an order of magnitude faster than previously reported for activation of Ni_u-A states formed by O_2-sensitive hydrogenases the faster value is consistent with a reactivation process where the active site states change in a stepwise fashion transitioning through the intermediates with the same rate determining step.[2,61] Taking this data together, we assign the ν_{CO} bands in the IR absorption spectrum of our as-isolated *Ec*Hyd-1 sample to a mixture of Ni_r-$S_{I/II}$ (1908, 1922 cm^{-1}) and Ni_r-B (1942 cm^{-1}) in which the population of the 1922 cm^{-1} state accounts for approximately 60% of the total.

Turning to the ν_{CN} region of the spectrum, we observe that the as-isolated sample features bands at 2050 and 2063 cm^{-1} (Fig. 3(a), black, Fig. S1 and S2, ESI†). It is noticeable that these too are very similar to the values reported for the Ni_a-SR_{II} state, suggesting further coincidence with this state.[33] However, it is not possible to directly link the ν_{CO} and ν_{CN} signals for the individual states using IR absorption spectroscopy and so we turn to 2D-IR spectroscopy for this as well as a more in-depth analysis of the spectroscopy, structure and dynamics of the states that we will henceforth refer to as Ni_r-$S_{I/II}$. IR absorption

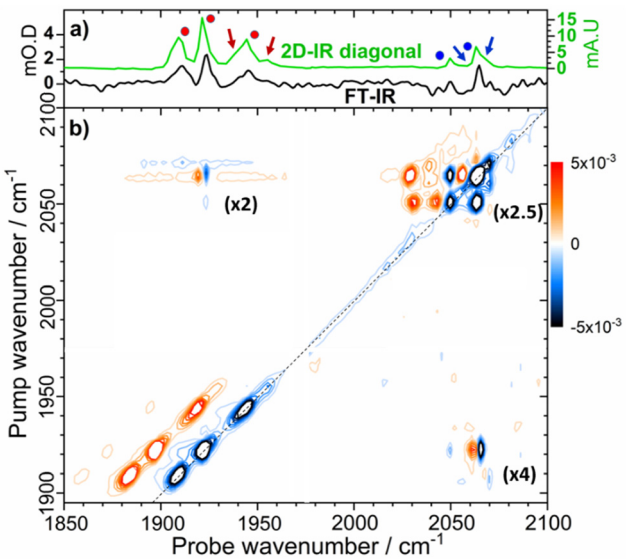

Fig. 3 (a) IR absorption spectrum of as-isolated *Ec*Hyd-1 (black trace) and projection of the 2D-IR spectrum diagonal (green). The negative signals of the diagonal have been inverted for comparison with the IR absorption spectrum. (b) 2D-IR spectrum of as-isolated *Ec*Hyd-1 recorded at a waiting time (T_w) of 250 fs. The dashed line indicates the spectrum diagonal. Numbers in brackets indicate the magnification of the three quadrants of the 2D-IR spectrum containing peaks due to ν_{CN} modes in relation to the ν_{CO} region of the spectrum (1900–1950 cm^{-1}), which contains the most intense peaks. See text for explanation of blue/red dots and arrows.

measurements made as a function of pH showed that more basic conditions favoured the active site state with a ν_{CO} band at 1922 cm^{-1}, which suggests that an assignment to the deprotonated Ni_r-S_I state may be most likely. However, it is not possible to differentiate definitively between states labelled

I or II and so we will refer them as Ni_r-$S_{I/II}$ and identify individual states by the ν_{CO} frequency if required.

Comparison of 2D-IR and IR absorption spectra. The 2D-IR spectrum of the as-isolated *Ec*Hyd-1 sample shows a large number of diagonal and off-diagonal peaks (Fig. 3(b)). The ν = 0–1 (fundamental) transitions of vibrational modes that are observed as bands in the IR absorption spectrum appear as negative peaks along the diagonal of the 2D-IR spectrum (dashed line). These ν = 0–1 transitions from Fig. 3(b) are inverted and reproduced (Fig. 3(a), green) alongside the IR absorption spectrum (black) for comparison. All the ν_{CO} and ν_{CN} bands appear on the 2D-IR spectrum diagonal (Fig. 3(a) (green)). The third order non-linear nature of the 2D-IR experiment, which enhances signals from modes with large extinction coefficients relative to those of weaker, broad features means that the 2D-IR spectrum is free from the effects of the water combination band near 2100 cm^{-1}, removing the need for any solvent correction (Fig. S1, ESI†).[48,49,62,63] Moreover, 2D-IR spectroscopy produces a somewhat narrower linewidth than IR absorption methods, leading to improved resolution of peaks.[48] The 2D-IR spectrum diagonal features the major ν_{CO} bands at 1908, 1922 and 1942 cm^{-1} (Fig. 3(a), red circles) and shows a high frequency band at 1955 cm^{-1} along with a shoulder visible at 1938 cm^{-1} (red arrows in Fig. 3(a)).

In the ν_{CN} region of the 2D-IR spectrum, bands at 2050 and 2063 cm^{-1} are present (Fig. 3(a), blue circles). In addition, a high frequency shoulder on the 2063 cm^{-1} band is also clearly observed, with the indication of another weaker band between those at 2050 and 2063 cm^{-1} (minor bands are highlighted by blue arrows in Fig. 3(a)). We discuss these alongside other, less prominent, peaks in more detail below.

2D-IR peak assignments – ν_{CO} region. While the ν = 0–1 transitions of vibrational modes cause diagonal peaks in a 2D-IR spectrum, off-diagonal peaks provide additional information regarding the nature of the potential energy surfaces of the vibrational modes and their interactions. The three dominant negative peaks on the 2D-IR diagonal at 1908, 1922 and 1942 cm^{-1} (Fig. 4, blue) are not linked by off-diagonal peaks below the diagonal of the spectrum. The lack of such peaks precludes vibrational coupling of the ν_{CO} modes, or energy transfer between them as would be expected if they were due to three ν_{CO} modes of a single molecular unit. The observed peak pattern is therefore consistent with the above assignment of the three bands to the ν_{CO} stretching vibrations of three individual active site states of *Ec*Hyd-1: Ni_r-$S_{I/II}$ (1908, 1922 cm^{-1}) and Ni_r-B (1942 cm^{-1}).[27] Furthermore, we observe no evidence for exchange or interconversion of these states on timescales up to 45 ps, as this too would have given rise to off-diagonal peaks in this region of the spectrum.[64]

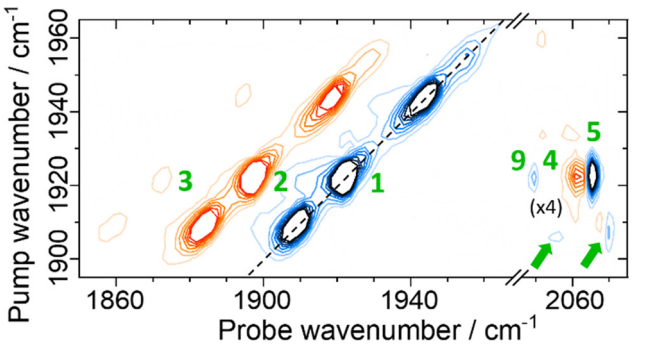

Fig. 4 Magnification of the 2D-IR spectrum of *Ec*Hyd-1 shown in Fig. 3(b) for pump frequencies coinciding with ν_{CO} bands. The spectrum was measured with a T_w of 250 fs. Green numbers refer to peak assignments and green arrows highlight minor off diagonal peaks as discussed in the text.

Each of the three main ν_{CO} diagonal peaks (1908, 1922 and 1942 cm^{-1}) is accompanied by a strong positive (red) peak shifted by ~25 cm^{-1} to lower probe frequency, with a second, much weaker positive peak shifted by the same amount again (Fig. 4). These are exemplified for the 1922 cm^{-1} (Ni_r-$S_{I/II}$) diagonal peak by green peak labels **1**, **2** and **3** in Fig. 4. The population of higher-lying vibrational levels by the pump pulse in the 2D-IR experiment allows the probe pulse to access transitions that are not observed using IR absorption methods at room temperature and so peaks **1–3** can be assigned to the ν = 0–1, ν = 1–2 and ν = 2–3 transitions of the ν_{CO} mode respectively. The smaller diagonal peaks at 1955 and 1938 cm^{-1} also have an accompanying ν = 1–2 transition, with similar anharmonicities to those of the larger bands suggesting that these too are assignable to ν_{CO} modes of two more active site states present in lower concentrations than those which give rise to the main bands.

The ν = 0–1, ν = 1–2 and ν = 2–3 transition frequencies for each of the three most intense ν_{CO} modes were found to be well-represented by Morse anharmonic oscillator functions (Fig. S7 and S8, ESI†). The spectroscopic constants derived in each case are shown in Table S1 of the ESI.† The transitions and all peak assignments for the Ni_r-$S_{I/II}$ (ν_{CO}: 1922 cm^{-1}) state of *Ec*Hyd-1 are summarized in a representative energy level diagram (Fig. 5) showing the ν_{CO} and ν_{CN} energy levels (*vide infra*). We confirm below that each observed state of *Ec*Hyd-1 is associated with one ν_{CO} and two ν_{CN} modes, as would be expected,[65] and so we introduce vibrational state designations using the notation $|\nu_{CO}\nu_{CN1}\nu_{CN2}\rangle$, where CN1 and CN2 indicate the higher and lower frequency ν_{CN}-modes, respectively. Using this notation peaks **1–3** are identified as: $|000\rangle$–$|100\rangle$; $|100\rangle$–$|200\rangle$; $|200\rangle$–$|300\rangle$.

A further set of off-diagonal peaks with a pump frequency of 1922 cm^{-1} but with probe frequencies ranging between 2050 and 2063 cm^{-1} are present in the 2D-IR spectrum (Fig. 4, **4**, **5** and **9**). The most intense of these is a negative peak, **5**, with frequency coordinates (pump, probe) = (1922, 2063 cm^{-1}). The pump frequency matches one of the ν_{CO} bands assigned to Ni_r-$S_{I/II}$ while the probe frequency coincides with a diagonal peak in the ν_{CN} region of the spectrum. As the 2D-IR spectrum in Fig. 4 was obtained with a waiting time (T_w) of 250 fs, this off-diagonal peak indicates that these ν_{CO} and ν_{CN} modes are vibrationally coupled. A weaker negative peak at (1922, 2050 cm^{-1}), **9**, shows that the ν_{CO} band of this Ni_r-$S_{I/II}$ state is associated with a pair of ν_{CN} modes with frequencies of 2050 and 2063 cm^{-1}. This enables an unambiguous assignment of a

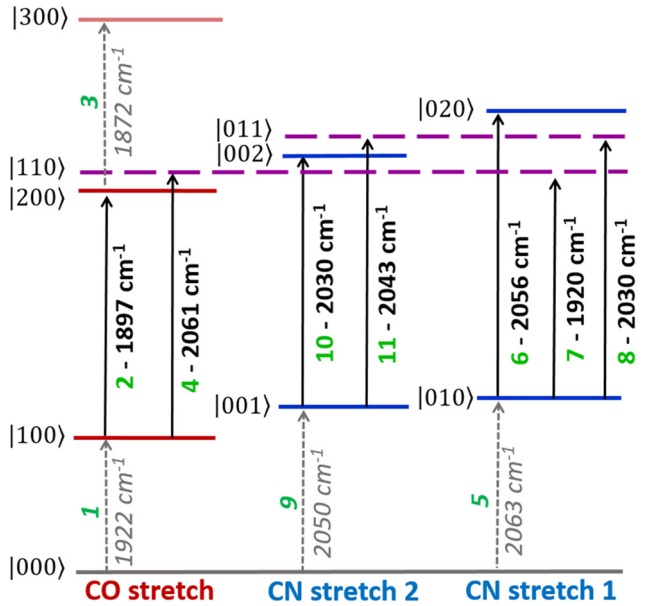

Fig. 5 Energy level diagram showing vibrational energy levels $|\nu_{CO}\nu_{CN1}\nu_{CN2}\rangle$ and transition wavenumbers of the ν_{CO} and ν_{CN} vibrational manifold, as detected for the active site state of *Ec*Hyd-1 with a ν_{CO} fundamental frequency of 1922 cm^{-1} (Ni_r-$S_{I/II}$). Transitions are labelled with green numbers used to identify peak assignments in the 2D-IR spectra (see text).

set of ν_{CO} and ν_{CN} mode frequencies to one of the Ni_r-$S_{I/II}$ active site states of *Ec*Hyd-1, consistent with the presence of a $Fe(CO)(CN)_2$ unit.

The strong positive peak (**4**), which has the same pump frequency (1922 cm^{-1}) but a probe frequency of 2061 cm^{-1} is assigned to a transition between the $v = 1$ level of the ν_{CO} mode ($|100\rangle$) populated by the pump pulse, and a combination state featuring one quantum of energy in both the ν_{CO} and the high frequency ν_{CN} stretching vibrations ($|110\rangle$). The separation of peaks **5** and **4** along the probe frequency axis in Fig. 4 indicates the mixed mode anharmonicity of the combination band.[48,66,67] The mixed mode anharmonicity is the amount by which the combination band frequency is shifted relative to the sum of the fundamental transitions of the two participating modes and is a measure of coupling strength of the ν_{CO} and ν_{CN} modes. In this case, a shift of ≤ 2 cm^{-1} indicates weak ν_{CO} to ν_{CN} coupling. These assignments are shown in the energy level diagram in Fig. 5.

Closer examination of Fig. 4 shows a second pair of off-diagonal peaks (green arrows in Fig. 4) linking the Ni_r-$S_{I/II}$ ν_{CO} mode at 1908 cm^{-1} with the ν_{CN} modes at 2057 and 2070 cm^{-1}. These peaks are weak, and the associated positive peaks are not clearly visible, but they indicate the set of coupled ν_{CO} and ν_{CN} modes that correspond to the Ni_r-$S_{I/II}$ state (ν_{CO}: 1908 cm^{-1}) of *Ec*Hyd-1.

A number of off-diagonal peaks are present in the upper left quadrant of Fig. 3(b). These are the reverse of the peaks in the bottom right of the plot, which were discussed above (Fig. 3(b) and 4), in that the pump frequency now coincides with the ν_{CN} diagonal peaks, and the off-diagonal peaks link ν_{CN} and ν_{CO} modes. The peaks in this region include the peak marked **7** in Fig. 5 (2063, 1920 cm^{-1}) and are consistent with the coupling patterns identified above, further confirming the linked sets of ν_{CO} and ν_{CN} modes.

2D-IR peak assignments – ν_{CN} region. The 2D-IR spectrum near the ν_{CN} diagonal peaks is expanded in Fig. 6 and shown at a range of waiting times. This region of the spectrum contains three clear diagonal peaks at frequencies of 2050, 2063 and 2070 cm^{-1} and a weaker peak at 2057 cm^{-1} which is visible as a shoulder on the 2063 cm^{-1} band (Fig. 6(a)). These peaks have been shown by ν_{CO} to ν_{CN} coupling to be assignable to the cyanide stretching frequencies of two separate Ni_r-$S_{I/II}$ active site states (ν_{CO}, ν_{CN2}, ν_{CN1}: 1922/2050/2063 cm^{-1} and 1908/2057/2070 cm^{-1}).

The rich off-diagonal peak structure in the ν_{CN} region can be used to construct an energy level diagram for these modes up to states containing two quanta of vibrational energy ($v = 2$ or mixed mode combination states). We begin by focusing on the strongest ν_{CN} diagonal peak at 2063 cm^{-1} (Fig. 6(b), **5**). When pumping the 2063 cm^{-1} mode ($|000\rangle$–$|010\rangle$), three clear off-diagonal peaks are visible (**6**, **8** and **9′**; the prime indicates an off-diagonal peak arising from transition **9** in Fig. 5 to differentiate it from a diagonal peak which is identified by the same number below). The positive peak **6** is assigned to the $v = 1$–2 transition of the ν_{CN} vibrational mode ($|010\rangle$–$|020\rangle$). This shows a single mode anharmonic shift of 8 cm^{-1} relative to the fundamental transition ($|000\rangle$–$|010\rangle$).

Negative peak **9′** indicates that the ν_{CN} modes at 2063 cm^{-1} and 2050 cm^{-1} are vibrationally coupled, consistent with the identification above that these two modes arise from the same single Ni_r-$S_{I/II}$ state. It is important to note that the 2063 cm^{-1} diagonal peak only shows coupling to one other ν_{CN} mode, as would be expected for a $Fe(CO)(CN)_2$ unit.

Peak **8** (positive) arises from a transition to the combination state featuring one quantum of excitation in each of the ν_{CN} modes at 2050 and 2063 cm^{-1} ($|010\rangle$–$|011\rangle$). These transitions are marked on the energy level diagram in Fig. 5. The large separation of peaks **8** and **9′** shows that the mixed mode anharmonicity of the $|011\rangle$ combination band is 20 cm^{-1}, indicating that the two ν_{CN} modes are much more strongly coupled to each other than to the ν_{CO} modes.

The diagonal ν_{CN} peak at 2050 cm^{-1} (Fig. 6(b), **9**) corresponding to the fundamental transition of the second ν_{CN} mode of the Ni_r-$S_{I/II}$ state, is also accompanied by three off-diagonal peaks. Peak **5′** reflects the coupling to the ν_{CN} mode at 2063 cm^{-1} as expected. Assignment of the positive peaks **10** and **11** is less straightforward. An initial assignment of peak **11** to the $v = 1$–2 transition of the 2050 cm^{-1} ν_{CN} mode might be expected. However, consideration of the energy level diagram (Fig. 5) shows that the unusually large mixed mode anharmonicity (20 cm^{-1}) arising from the strong coupling of the two ν_{CN} modes leads to the positive partner expected near peak **5′** for a pair of coupled modes appearing on the opposite side of the spectrum diagonal from **5′**. As a result, the correct assignment of peak **11** is to the transition to the combination state of the two ν_{CN} modes ($|001\rangle$–$|011\rangle$), Fig. 5). This means that peak **10**

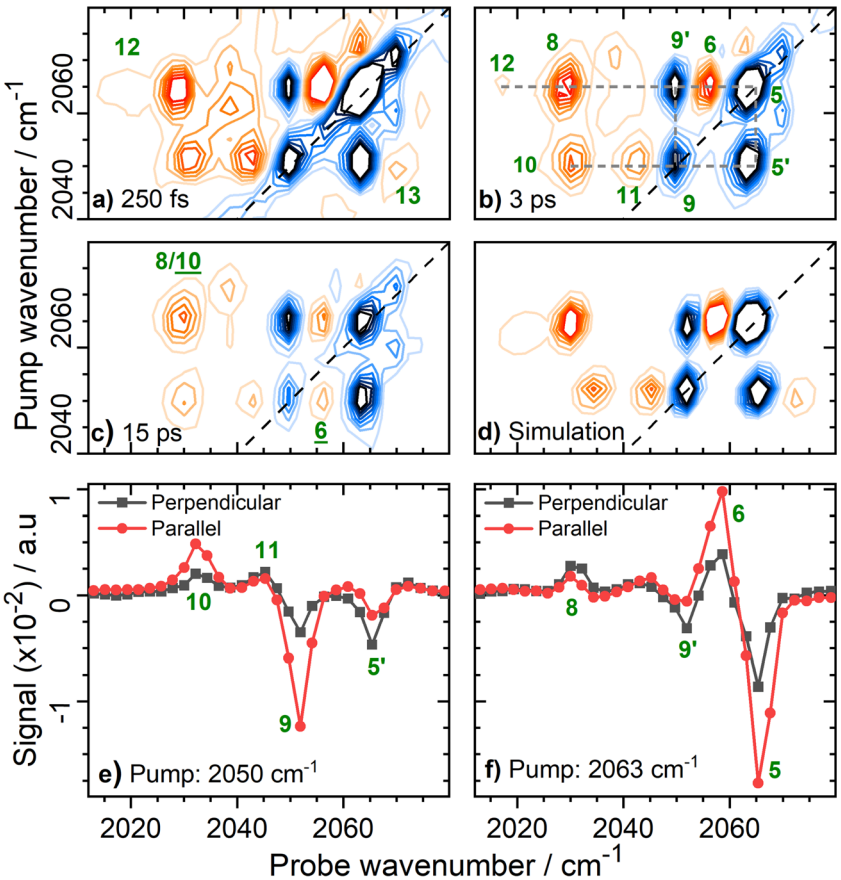

Fig. 6 Magnification of the 2D-IR spectrum of *Ec*Hyd-1 from Fig. 3(b) for pump frequencies coinciding with ν_{CN} bands at a series of values of T_w. (a) T_w = 250 fs with forbidden transitions, **12** and **13** highlighted; (b) T_w = 3 ps with full peak assignment for the major set of coupled ν_{CN} modes (dashed grey lines); (c) T_w = 15 ps showing energy transfer peaks, **6** and **10** (d) Simulated 2D-IR spectrum (see text) for the major pair of coupled CN modes with fundamental transition frequencies of 2050 and 2063 cm^{-1}. (e and f) Slices through the 2D-IR spectrum shown in (b) under parallel (red) and perpendicular (black) polarization conditions. The pump frequency in each case is given in the legend.

is assigned to the ν = 1–2 transition of the 2050 cm^{-1} ν_{CN} mode, ($|001\rangle$–$|002\rangle$), an anharmonic shift of 20 cm^{-1} that is significantly different to the value of 8 cm^{-1} identified for the 2063 cm^{-1} mode.

Our peak assignments in the ν_{CN} region are supported by examining the 2D-IR spectrum at longer waiting times. Fig. 6(c) shows an additional peak, **6** (the underline is used to identify a peak appearing at later waiting times), which becomes visible at coordinates of (pump, probe) (2050, 2058 cm^{-1}) at waiting times approaching ~15 ps. The delayed arrival of this peak along with its position indicates that it is due to energy transfer from the ν = 1 state of the excited (pumped) ν_{CN} mode at 2050 cm^{-1} ($|001\rangle$), to the ν = 1 level of the ν_{CN} mode at 2063 cm^{-1} ($|010\rangle$). The probe pulse is then able to excite the ($|010\rangle$–$|020\rangle$) transition of the 2063 cm^{-1} mode, which lies at 2058 cm^{-1} (Fig. 5). Peak **6** is thus assigned to the effects of energy transfer between the two ν_{CN} modes. The timescale is consistent with the relaxation dynamics of the ν = 1 levels of the ν_{CN} modes (*vide infra*). The reverse peak, featuring energy transfer from the pumped 2063 cm^{-1} mode to the 2050 cm^{-1} mode followed by the probe exciting the ($|001\rangle$–$|002\rangle$) transition would be expected at (2063, 2030 cm^{-1}). This position coincides almost exactly with peak **8**, which is assigned to the effect of vibrational coupling. However, the persistence of peak **8** to a waiting time of at least 45 ps, in contrast to the other peak arising from coupling (**11**), is consistent with the presence of overlapping peaks, one of which arises from energy transfer (**10**, Fig. S9, ESI†). The vibrational relaxation dynamics of the ν_{CO} and ν_{CN} modes are discussed in more detail below.

2D-IR measurements performed at different pump–probe pulse polarization geometries provide further support for our peak assignments in the ν_{CN} region of the spectrum as well as adding structural information relating to the *Ec*Hyd-1 active site in solution. Peaks **5**/**6** and **9**/**10** (Fig. 6(b)), which are assigned to ν = 0–1 and ν = 1–2 transitions of the high frequency and low frequency ν_{CN} modes of Ni_r-$S_{I/II}$ respectively, undergo significant reduction in amplitude upon changing from parallel to perpendicular relative pump–probe polarizations (Fig. 6(e) and (f)). This is as expected because the directions of the transition dipole moments associated with the ν = 0–1 and ν = 1–2 transitions of a given mode necessarily lie in the same direction. In contrast, the peaks arising from transitions involving combination states (**8** and **11**) show much weaker polarization dependence (Fig. 6(e) and (f)). This is consistent with a signal arising

from pump and probe events, which interact with vibrational modes whose transition dipole moments lie at right angles to each other.

Polarization-dependent 2D-IR measurements can also be used to quantify the angular relationship between the two ν_{CN} modes by determining the anisotropy parameters for the pairs of diagonal and off-diagonal peaks labelled **9**/**5′** in Fig. 6(b).[49] The values obtained, 0.45 (**9**) and −0.24 (**5′**) (Fig. S10, ESI†), are, within error, consistent with two vibrational modes with transition dipole moments oriented at 90° to each other, as expected for a *cis* geometry of the two cyanide ligands at the hexacoordinated Fe center.

The presence of strong coupling of the two ν_{CN} modes, as evidenced by a mixed mode anharmonicity (20 cm^{-1}) greater than the mode separation (13 cm^{-1}), would be expected to lead to the partial breakdown of vibrational selection rules ($\Delta\nu$ = ±1), enabling transitions from the ν = 1 level of one ν_{CN} mode to the ν = 2 level of the second, (*e.g.* $|001\rangle$–$|020\rangle$), which would formally be forbidden.[48] For the Ni_r-$S_{I/II}$ (ν_{CO}: 1922 cm^{-1}) state these transitions are predicted by the energy level diagram in Fig. 5 to lie at (pump, probe) (2050, 2071 cm^{-1}) and (2063, 2017 cm^{-1}) and they can clearly be observed in Fig. 6(a), labelled **12** ($|001\rangle$–$|020\rangle$) and **13** ($|010\rangle$–$|002\rangle$) respectively. The presence of these features adds further weight to our assignments. The energy level diagram in Fig. 5 was used to construct a simulation of the ν_{CN} region of the 2D-IR spectrum based on 2D-Gaussian functions (see ESI,† for details). This is shown in Fig. 6(d) and the agreement with the experimental data is excellent.

In addition to the set of peaks arising from the pair of ν_{CN} modes at 2050 and 2063 cm^{-1}, a second much less intense set of peaks can be observed linking the coupled pair of ν_{CN} modes due to the Ni_r-$S_{I/II}$ (ν_{CO}: 1908 cm^{-1}) state at 2070 and 2058 cm^{-1}. These are shown in Fig. 7, labelled **(5)**/**(5′)**, **(6)**, **(8)**, **(9)**/**(9′)** and **(10)**, showing that the ν_{CN} spectroscopy of the two different active site states is very similar.

Vibrational relaxation dynamics. The vibrational relaxation dynamics of the ν_{CO} and ν_{CN} modes of *Ec*Hyd-1 were determined *via* an IR_{pump}–IR_{probe} spectroscopy experiment on the as-isolated sample (Fig. 8(a)). Three strong negative features are visible in the ν_{CO} region of the spectrum, assignable to the ν = 0–1 transitions of bands of the three main active site states (Ni_r-$S_{I/II}$ and Ni_r-B). Positive features due to the ν = 1–2 transitions are also visible, but we have shown that these are better identified in the 2D-IR spectrum, which removes any ambiguity in the assignments caused by overlapping peaks. The vibrational lifetimes for the ($|100\rangle$ states were obtained by fitting the time dependences of the respective peak intensities using single exponential decay functions (Fig. 8(b)). Values of between 16 ± 3 and 25 ± 3 ps for the three states were obtained (Table S2, ESI†).

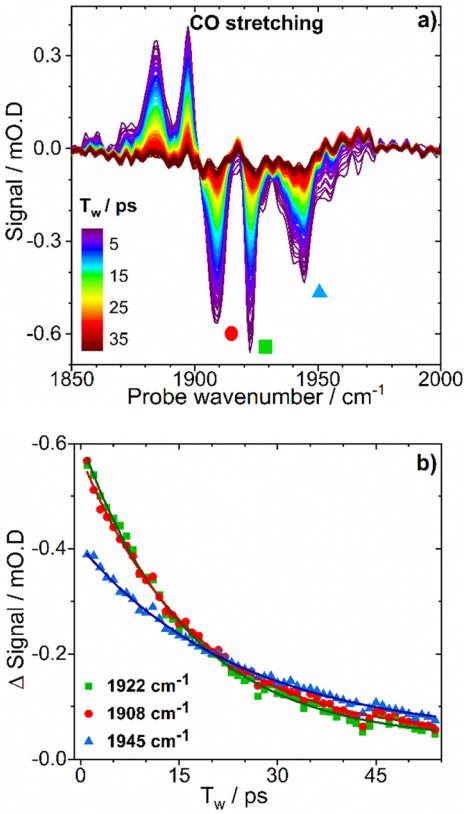

Fig. 8 (a) IR_{pump}–IR_{probe} spectra of as-isolated *Ec*Hyd-1in the ν_{CO} region of the spectrum. (b) Plots of band intensity *versus* time for selected bands from the spectra in (a), each identified by colored symbols. Solid lines show results of fitting experimental data with monoexponential decay functions.

The vibrational lifetimes of the three most intense ν_{CN} modes, with fundamental transitions located at 2050, 2063 and 2070 cm^{-1} were 32 ± 2, 37 ± 2 and 29 ± 2ps respectively (Table S2 and Fig. S11, ESI†). These values of the vibrational lifetimes for the carbonyl and cyanide modes are consistent with peaks due to energy transfer between ν_{CN} modes, which appear in the 2D-IR spectra at waiting times of ~15 ps (Fig. 6(c)). Similarly, a peak was observed in the 2D-IR spectrum at coordinates of (pump, probe) = (2063, 1897), which can be assigned to energy transfer from the pumped ν_{CN} ($|010\rangle$) level of Ni_r-$S_{I/II}$ (ν_{CO}: 1922 cm^{-1}) to the ν_{CO} ($|100\rangle$, leading to the probe exciting the $|100\rangle$–$|200\rangle$ transition of the ν_{CO} mode (**2**, Fig. S12, ESI†).

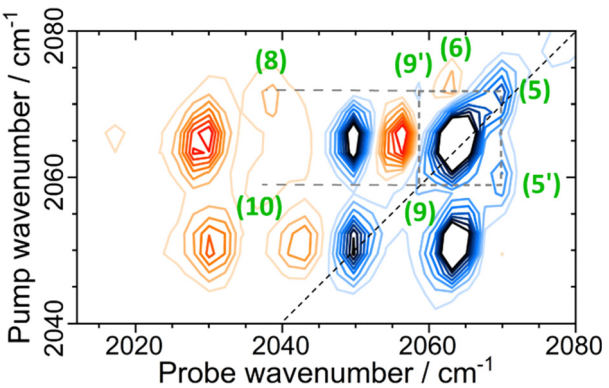

Fig. 7 2D-IR spectrum of *Ec*Hyd-1 at T_w = 250 fs in the ν_{CN} region of the spectrum, with full peak assignment for the minor set (dashed lines) of coupled CN modes due to the Ni_r-$S_{I/II}$ state.

Structural dynamics – 2D-IR diagonal lineshapes. The 2D-IR spectra of *Ec*Hyd-1 can also be used to provide information relating to structural dynamics near the active site *via* changes in the 2D-lineshapes of the diagonal peaks of the ν_{CO} and ν_{CN} modes with waiting time. If dynamic fluctuations of the local environment near a ligand give rise to a range of different structural microenvironments, each with a slightly different vibrational frequency, the band will display inhomogeneous broadening. This broadening is manifest as a Gaussian lineshape in the IR absorption spectrum. In the 2D-IR spectrum, inhomogeneous broadening affects the diagonal width of the ν_{CO} and ν_{CN} fundamental peaks while the antidiagonal linewidth reflects the homogeneous linewidth. This causes a diagonal elongation of the 2D peaks for inhomogeneously-broadened modes.[48] If the local structural dynamics causing the inhomogeneous broadening are occurring on timescales similar to, or shorter than, the vibrational relaxation time of the mode, then the 2D lineshape evolves from diagonally-elongated to circular as the waiting time increases. This change in lineshape occurs because structural dynamics lead to the excited mode being able to explore all of its available microenvironments within the pump–probe delay time; a process called spectral diffusion.[47] Observing the time-dependent evolution of the 2D lineshape *via* the ratio of diagonal to antidiagonal linewidths leads to an indication of the extent and timescales local environmental fluctuations.

In the case of *Ec*Hyd-1 the ν_{CO}, ν_{CN1} and ν_{CN2} bands exhibited ratios of the diagonal to antidiagonal full width half maximum values of 1.7, 1.6 and 1.5 respectively at a waiting time of 250 fs. These values were unchanged at a waiting time of 15 ps, indicating little in the way of structural dynamics occurring on timescales between 200 fs and 15 ps.

Examination of the dephasing time of the ν_{CO} mode of the 1922 cm^{-1} peak (4 ps) suggests an expected homogeneous linewidth of 3 cm^{-1}. Together with the observed diagonal linewidth (5 cm^{-1}) for this mode, this is consistent with the observed diagonal : antidiagonal width ratio of 1/7 (=5/3) and also indicates a very limited degree of inhomogeneous broadening.

Other active site states. To investigate the state-dependence of the observed spectroscopic and dynamic parameters, 2D-IR spectroscopy was performed on an O_2-exposed sample of as isolated *Ec*Hyd-1 to enhance the peaks due to the Ni_r-B state (Fig. S13 and S14, ESI†). This allowed identification of a set of bands due to the $\nu = 0$–1 transitions of the ν_{CO}, ν_{CN1} and ν_{CN2} modes at 1942, 2092 and 2080 cm^{-1} respectively as well as to determine the associated energy level diagrams up to and including the two quantum vibrational states (Fig. S14, ESI†). It is noteworthy that the Ni_r-B state, which features a Ni^{III} center, exhibits anharmonicities and spectral features that are very similar to those of the Ni_r-$S_{I/II}$ states described in detail above. The structural and vibrational dynamics were also observed to be similar to those reported for the Ni_r-$S_{I/II}$ states. This is consistent with the similar structural features assumed for all three states (Fig. 1(a)).

The O_2-oxidised sample of *Ec*Hyd-1 also gave rise to another set of ν_{CO}, ν_{CN1} and ν_{CN2} bands at 1948, 2098 and 2080 cm^{-1}, which we tentatively assign to the Ni_u-S states (Fig. 1(a) and Fig. S14, ESI†). In the case of this set of bands, it is notable that the positions are somewhat different, with evidence for the single mode anharmonicity of the higher frequency ν_{CN} band being as high as 13 cm^{-1}, while the mixed mode anharmonicity is reduced to 13 cm^{-1} (Table S3 and Fig. S14, ESI†). These changes may be attributable to the presence of a bridging sulphoxygenated cysteine residue in the active site structure (Fig. 1(a)).

Model compound: $K[CpFe(CO)(CN)_2]$

To provide a direct insight into the influence of the protein scaffold on the spectroscopy of the enzyme active site, we measured the 2D-IR spectrum of the model compound $K[CpFe(CO)(CN)_2]$ (**M1**) in aqueous solution.[68,69]

The results (Fig. 9(a)) show the spectral band patterns observed for **M1** are broadly similar to those of the enzyme

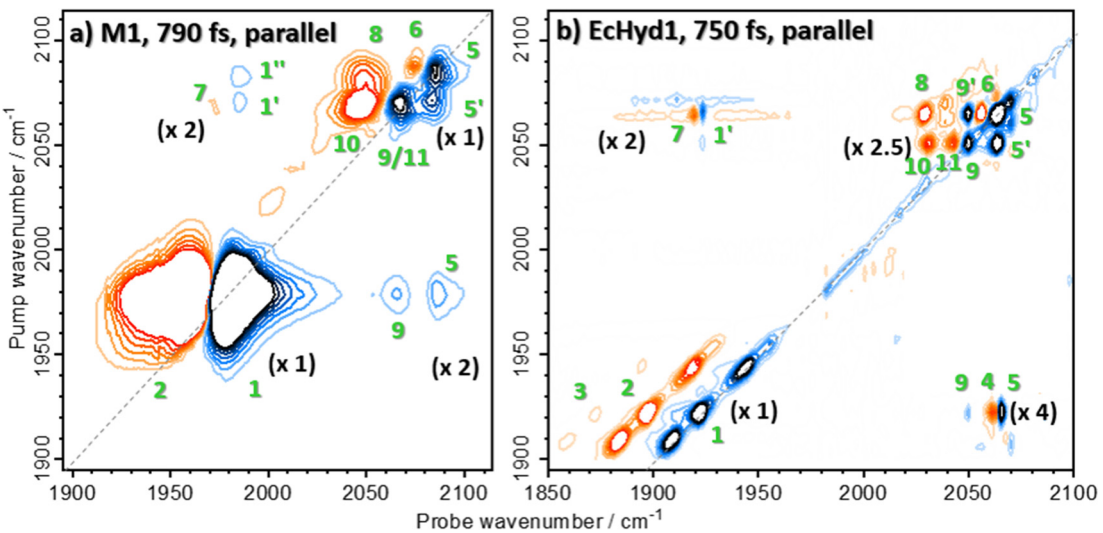

Fig. 9 2D-IR spectra of (a) compound **M1** in H_2O solution and (b) as isolated *Ec*Hyd-1 obtained for similar values of T_w.

(reproduced in Fig. 9(b)) allowing similar assignments of the peaks to be made. This approach shows that the anharmonicity of the ν_{CO} mode of **M1** is 24 cm^{-1} and that this mode is weakly coupled to the ν_{CN} modes (mixed mode anharmonicity: $\leq$5 cm^{-1}). The two ν_{CN} modes of **M1** show quite different single mode anharmonicities to one another (10 and 22 cm^{-1}), while the mixed mode anharmonicity for the ν_{CN} modes of **M1** was found to be 19 cm^{-1}.

Examining the spectral linewidths and structural dynamics of the ν_{CO} and ν_{CN} modes shows that the ν_{CO} and ν_{CN} bands of **M1** dissolved in H_2O are much broader than those in the enzyme. The ν_{CO} band of **M1** has a diagonal linewidth of 20 cm^{-1} as compared to 8, 5 and 12 cm^{-1} for the *Ec*Hyd-1 states at 1908, 1922 and 1942 cm^{-1} respectively. In the case of the ν_{CN} bands, widths of 12 and 14 cm^{-1} (**M1**) compare with 5 cm^{-1} for the enzyme, irrespective of the active site state. The 2D lineshapes of **M1** in solution were observed to undergo rapid spectral diffusion, with the ratios of the diagonal to antidiagonal linewidths changing from 1.5, 1.2 and 1.5 (ν_{CO}, ν_{CN1}, ν_{CN2}) at short T_w (125 fs) to values of unity by a waiting time of 2 ps. This indicates that rapid structural fluctuations are present in solution that do not influence the 2D lineshapes of the enzyme. Finally, the vibrational relaxation dynamics of the ν_{CO} and ν_{CN} modes of **M1** (4 and 6/7 ps respectively (Fig. S15, ESI†)) are significantly faster than those of *Ec*Hyd-1 Ni_r-$S_{I/II}$ (16–25 ps and 29–37 ps respectively).

Discussion

Applying 2D-IR spectroscopy alongside a suite of enzyme characterization measurements has enabled identification of ν_{CO} and ν_{CN} frequencies for two previously un-reported active site states of *Ec*Hyd-1, Ni_r-$S_{I/II}$ in addition to data on two other active site states. The 2D-IR spectra have also provided deeper insights into the vibrational potentials of the ν_{CO} and ν_{CN} bands of these states while the sub-picosecond time resolution has been exploited to reveal their vibrational and structural dynamics.

Our observations show that the spectroscopy and dynamics of all of the active site states of *Ec*Hyd-1 studied so far are broadly similar, with the exception of some minor deviation for signals assigned to the Ni_u-S state. It is therefore interesting to consider whether this extends to other [NiFe] hydrogenases *via* our previous study of the *Re*RH enzyme.[52] The vibrational relaxation and structural dynamics reported for *Re*RH were very similar to those observed for *Ec*Hyd-1, (ν_{CO} and ν_{CN} vibrational lifetimes were 18 and 30 ps respectively[52]) along with no evidence of significant structural changes occurring on this timescale as evidenced by spectral diffusion measurements. Although the ν_{CN} region of the 2D-IR spectrum of *Re*RH was less well-resolved than reported for the *Ec*Hyd-1 enzyme studied here, revisiting the *Re*RH 2D-IR spectroscopy in light of our new results allows a clearer picture to emerge. An early waiting time 2D-IR spectrum of the *Re*RH enzyme in the ν_{CN} region is presented (Fig. 10(a)) alongside a simulation based on a similar

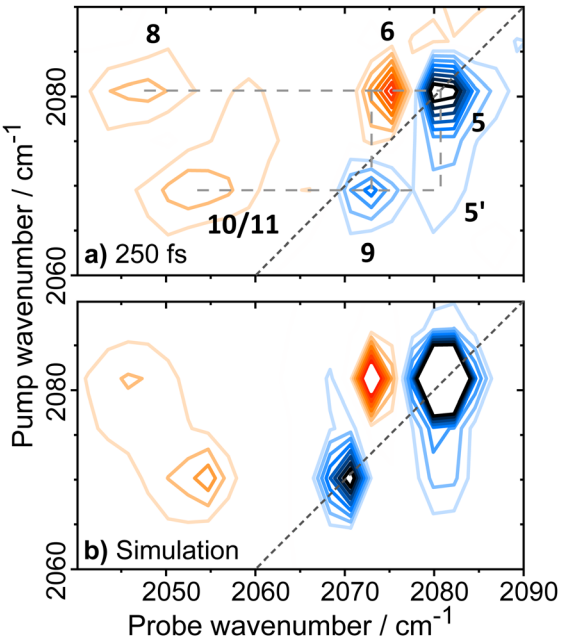

Fig. 10 (a) 2D-IR spectrum of *Re*RH with pump frequencies resonant with ν_{CN} modes obtained with a T_w of 250 fs; (b) simulation of the *Re*RH 2D-IR spectrum in the ν_{CN} region based on a similar set of vibrational states as determined for *Ec*Hyd-1.

mode structure and energy level diagram (Fig. S16, ESI†) to that observed for *Ec*Hyd-1 (Fig. 10(b)). The agreement is excellent, allowing us to define single mode (8 and 18 cm^{-1}) and mixed mode (24 cm^{-1}) anharmonicities for the *Re*RH ν_{CN} modes (Table S3, ESI†) that are very similar to the values for *Ec*Hyd-1. This new information also allows complex time-evolution behavior of the peaks observed in the *Re*RH spectra[52] to be assigned to the differential relaxation of combination band and energy transfer peaks as described for *Ec*Hyd-1 above (Fig. S17, ESI†). This result strongly suggests that the active sites of the two enzymes which perform quite different biological functions have common characteristics to their $Fe(CO)(CN)_2$ units.

We now proceed to consider how the results for the enzyme active site compare to those of a structural mimic of the $Fe(CO)(CN)_2$ unit in aqueous solution. Our results for the enzyme show that while the spectroscopy of the ν_{CO} bands of the Ni_r-$S_{I/II}$ states are well-described by a Morse-oscillator model, the ν_{CN} bands show some unusual characteristics. In particular, the two ν_{CN} bands exhibit markedly different single mode anharmonicities, one with a value of 20 cm^{-1}, while the other is much less anharmonic (8 cm^{-1}). The vibrational coupling of the ν_{CN} modes is indicated by the observed mixed mode anharmonicity value of 20 cm^{-1}. Although vibrational coupling of the ν_{CN} modes in hydrogenases has been detected previously,[52,70] our results here suggest that it is very strong, and sufficient to cause a breakdown in harmonic oscillator selection rules that results in the observation of peaks **12** and **13** in Fig. 6(a). It is important to stress that these effects cannot be explained using a harmonic description of the potential energy surfaces of the CN bonds, rather, they arise

from the higher order, cubic and quartic terms, the effects of which are not discernable using absorption spectroscopy.[48,71–74]

Our results obtained from **M1** in solution show that some of the observations relating to the spectroscopy of the observed *Ec*Hyd-1 active site states can be attributed to the intrinsic nature of the $Fe(CO)(CN)_2$ unit. For example the single mode anharmonicity of the low frequency ν_{CN} mode as well as the mixed-mode anharmonicity are consistent between **M1** and the enzyme, the latter showing that the strong inter-ν_{CN} coupling is at least in part a feature of the $Fe(CO)(CN)_2$ unit. Further evidence indicating that the observed spectroscopic patterns are an intrinsic property of the $Fe(CO)(CN)_2$ can be found from other examples where single and mixed mode anharmonicities have been reported for organometallic cyanide-containing compounds, that also showed very different values to those of either **M1** or *Ec*Hyd-1.[75,76] However, the single mode anharmonicity observed for the high frequency ν_{CN} mode of *Ec*Hyd-1 is smaller than that of **M1** in solution, suggesting a degree of environmental sensitivity in this parameter. The ν_{CN} mode frequency separation is much less in *Ec*Hyd-1 ($\Delta\nu_{CN-CN}$ is 13 cm^{-1}) than **M1** (17 cm^{-1}), a change which brings the mode separation and mixed mode anharmonicities closer together for **M1**. This implies that **M1** approaches the weak coupling regime,[48] such that the forbidden transitions observed in the enzyme do not appear in spectra of **M1**. These results suggest that our observed spectroscopic differences between **M1** and the enzyme stem from the environment of the active site dictated by the protein scaffold. It is however important to note that, although the size and position of the Cp ring enables **M1** to provide a good structural mimic of the $Fe(CO)(CN)_2$ unit,[68,69] **M1** does not replicate either the Ni or the terminal and bridging cysteine residues, which have been shown to strictly control the local geometry of the NiFe site, leading to asymmetry in the two cysteine bridges.[9,10,35,77] These differences could in principle influence the vibrational potentials of the cyanide ligands that lie *trans* to them.

Although the impact of the protein scaffold upon spectroscopic parameters of the $Fe(CO)CN)_2$ unit is subtle, the results from **M1** reveal that it has a significant impact upon its dynamics. The data for **M1** reveals vibrational relaxation times for the ν_{CO} and ν_{CN} modes of **M1** on the order of a few picoseconds, in good agreement with previous studies of organometallic carbonyls and cyanides in aqueous solution.[78,79] This rapid vibrational relaxation in water is attributed to spectral overlap of the ν_{CN} and ν_{CO} mode frequencies with the broad bend-libration combination band of H_2O near 2100 cm^{-1} leading to an efficient energy dissipation pathway to the solvent.[80] In contrast, much slower vibrational relaxation was observed for the ν_{CN} and ν_{CO} modes of *Ec*Hyd-1, which shows that bulk-like H_2O does not interact with the active site. Instead, the observed vibrational relaxation times for *Ec*Hyd-1 are more consistent with observations of organometallic compounds in protic organic solvents. The fact that such solvents are capable of hydrogen bonding could imply a role for the H-bond links between the protein scaffold and $Fe(CO)(CN)_2$ unit in determining the observed dynamics.[76]

Differences between the structural dynamics of the model compound and the enzyme were also observed. The 2D-IR diagonal peaks due to the ν_{CN} and ν_{CO} modes of **M1** display inhomogeneously broadened lineshapes and fast (1–2 ps) spectral diffusion, while the enzyme modes show limited evidence of inhomogeneous broadening and no spectral diffusion on timescales up to 45 ps. The contrasting behavior of **M1** can be explained by rapid fluctuations of the H-bonding environment around the ligands and is consistent with previous studies in aqueous solutions.[81] Examination of the 2D-IR data shows that the ν_{CO} mode of **M1** in solution exhibits a much shorter dephasing time than the enzyme (0.96 ps *vs.* 4 ps). This faster dephasing contributes to the increased linewidth observed for **M1** compared to the enzyme, but would lead to a homogeneous linewidth of 12 cm^{-1}, showing that the observed 20 cm^{-1} linewidth arises from a significant degree of inhomogeneous broadening. In contrast, the ν_{CO} mode of the enzyme (at 1922 cm^{-1}) has a much narrower linewidth with little inhomogeneous contribution. These observations agree with previous work on *Re*RH.[52]

In the case of the enzyme, crystallography data indicates that the two cyanide ligands are H-bonded to the Thr532 and Arg509 residues (Fig. 11)[57] which feature neutral and cationic side chains respectively. Fluctuations of the protein would therefore be expected to modulate the terminal charges on the CN ligands and so the ν_{CN} mode frequencies, leading to structural dynamics being manifest as inhomogeneous broadening and spectral diffusion of the ν_{CN} modes. By the same argument the CO ligand, which is not subject to H-bonds, could be expected to show different behavior to the CN ligand modes, but the behavior of the ν_{CO} and ν_{CN} bands is very similar, although fluctuations of the protein environment could impact upon the ν_{CO} mode frequency *via* an electrostatic, rather than specifically H-bonding, mechanism. It is instructive that the CO

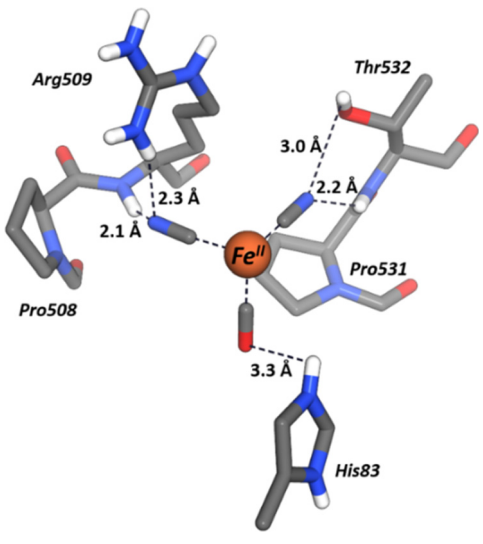

Fig. 11 Enlarged view of the *Ec*Hyd-1 active site $Fe(CO)(CN)_2$ moiety and its local environment, displayed as a ball and stick schematic. The image is from an X-ray crystal structure (PDB: 6FPW[57]) of an (18 hour) H_2-exposed sample of *Ec*Hyd-1. Distances to the hydrogen atoms are indicated.

and CN ligands of **M1** also demonstrate similar structural dynamics where again H-bonding would be expected to be stronger to the CN ligands, which would seem to support the hypothesis that the ligands detect similar environmental dynamics.

These observations could imply that the *Ec*Hyd-1 provides a very restricted environment with little fluctuation or that the fluctuations do not become manifest as spectral diffusion. However, these scenarios are not mutually exclusive and further study is required as it is not possible to be definitive from this data. An analysis of spectral linewidths and dephasing times performed on *Re*RH supported the presence of a dynamically rigid active site and the similarities between the data for *Re*RH and *Ec*Hyd-1 indicate that the same conclusions apply here.[52] Such a scenario would entail a protein scaffold that behaves in a markedly different manner to those revealed by studies of spectral diffusion in other protein and enzyme structures, where few picosecond spectral diffusion dynamics have been widely observed.[82–88] However, the role of the hydrogenases involves manipulating extremely small substrates as well as excluding slightly larger species such as water and so such a rigid architecture may be the biological solution to these complex problems. Another feasible explanation for the lack of observed spectral diffusion is that the H-bonding to the CN ligands is sufficiently weak that the cyanide ligand stretching frequencies do not act as an efficient reporter of protein motion. In this respect, the carbonyl ligand stretching mode frequency would appear to be similarly decoupled from protein fluctuations. If this were the case then it would be expected to have implications for the vibrational relaxation mechanism, the timescales of which are comparable with a protic, organic solvent. In the event of very weak hydrogen bonding, this could indicate that vibrational relaxation occurs *via* the dimetallic unit rather than through the protein.

Overall, we conclude that the enzyme active site dynamics, including both relaxation timescales and the lack of spectral diffusion, cannot be approximated by analogy to a single simple solvent model: the vibrational relaxation time points to a protic organic environment while the absence of spectral diffusion is more reminiscent of a non-interacting environment such as a non-polar organic solvent.[89,90] As such, the data indicates that the NiFe active site is subject to complex, multi-faceted influences but clearly communicates the importance of considering the protein scaffold as part of the active site. The evidence shows that the protein defines some aspects of the vibrational potential surfaces of the $Fe(CO)(CN)_2$ unit but that its major contribution is in defining the dynamic environment by effectively isolating the $Fe(CO)(CN)_2$ unit from the surrounding solvent and by either tightly controlling structural dynamics or limiting the impact of any fluctuations of the protein scaffold upon the active site.

Placing these results in context with the design of biomimetic hydrogen producing systems, the differences between our observations of the enzyme active site and measurements of model compound **M1** in solution indicate that further work assessing the contribution of the secondary coordination spheres, self-assembled scaffolds and/or full apo-enzymes have in effective hydrogenase biomimetic systems would be beneficial in developing artificial systems. While the role that the protein scaffold plays in the enzyme mechanism is not clear, the conserved nature of the local active site environment suggests that it is an important component of the hydrogenase architecture. Our results show that 2D-IR spectroscopy provides a facile route to characterizing attempts to replicate the biological scenario, in particular solvent exclusion and the complex structural dynamics, with simpler scaffolds.[11–18]

Finally, we reflect on the coincidence of the ν_{CO} and ν_{CN} mode frequencies for the Ni_r-$S_{I/II}$ states determined here at 1922/2050/2063 cm^{-1} and 1908/2057/2070 cm^{-1} (Table S2, ESI†) with those previously assigned to the Ni-R_{II} and Ni-R_{III}, (Ni_r-$SR_{II/III}$ using our notation) states which contain a hydride-bridged Ni(II)Fe(II) center (Fig. 1(a)).[27] Although the ν_{CO} mode frequency of the Ni_r-$S_{I/II}$ state (ν_{CO}: 1922 cm^{-1}) shows remarkable agreement with that assigned to Ni-R_{II}, that of the other Ni_r-$S_{I/II}$ state (ν_{CO}: 1908 cm^{-1}) differs from the literature values for the Ni-R_{III} state (ν_{CO}: 1914 cm^{-1}).[27] When added to the biochemical characterization data reported above, this discrepancy adds further weight to our assignment of the as-isolated *Ec*Hyd-1 spectrum to different states with coincident frequencies to one of the substates referred to as Ni-R.[27] The frequency coincidence extends to the ν_{CN} modes, which for both the Ni-R_{II} and Ni-R_{III} states were quoted as 2050 and 2067 cm^{-1},[27] while a recent study in the crystalline phase identified four bands between 2049 and 2071 cm^{-1}, though without direct assignment to the sub-states.[91] Thus the fact that we identify a similar set of frequencies as being attributable to a particular state is consistent with the Ni_r-$S_{I/II}$ and Ni-R_{II} and Ni-R_{III} states being spectroscopically very similar. There are in fact numerous reports of NiFe hydrogenases in distinct states exhibiting very similar IR signatures, for instance: Ni_r-B and Ni_u-A in *Allochromatium vinosum* MBH,[29] *Desulfovibrio vulgaris* Miyazaki F,[92] and *Desulfovibrio gigas MBH*;[93] and Ni_a-S and Ni_r-S in *Ralstonia eutropha* MBH[94] and RH,[95] and Ni_a-SR_{III} and Ni_a-SR_{II} of *Ralstonia eutropha* SH.[96] Finally, we note that the wavenumbers reported here for the Ni_r-$S_{I/II}$ states of *Ec*Hyd-1 fall within the range of reported frequencies for the same states of other enzymes (Fig. S18, ESI†).

Conclusions

We have reported the application of 2D-IR spectroscopy to study the active site of the *Ec*Hyd-1 enzyme, obtaining data for a number of active site states, including two previously un-reported Ni_r-$S_{I/II}$ states. By comparing the enzyme results to those of a model organometallic compound in aqueous solution, we reveal that the vibrational potential energy surfaces and dynamics of the $Fe(CO)(CN)_2$ unit, particularly of the ν_{CN} stretching modes, offer a sensitive probe of the local environment. The vibrational potential surfaces of the two CN ligand stretching modes are found to be quite different in terms of their single mode anharmonicities and they are

extremely strongly coupled. These observations are attributed partly to the nature of the $Fe(CO)(CN)_2$ unit, but also to a specific influence of the protein scaffold, which creates a highly specialized local environment by eliminating solvent from the active site and leading to dynamics that cannot be replicated using solvent analogs. The indication is of a protein scaffold that interacts surprisingly weakly with the active site or which very tightly controls the local structure *via* cysteine links to the NiFe centre and asymmetric H-bonding arrangement between the protein scaffold and the cyanide ligands. Further experiments targeting the specific interactions of the amino acids near the $Fe(CO)(CN)_2$ unit as well as investigating the potential role of vibrational relaxation phenomena such as IVR would be of benefit.[97,98]

A similar set of vibrational parameters, albeit with some evidence for state-to-state variations, can be used to describe the active sites of other [NiFe] hydrogenases studied so far, leading to the conclusion that the spectroscopic observables are indicative of an evolutionarily selected active site environment that is central to the enzyme structure, if not directly to its function. These observations demonstrate the need for the inclusion of anharmonic effects in understanding the potential energy surfaces of the active site vibrational modes, its structure, and dynamics. They also appear to explain the need for complex secondary coordination spheres in promising biomimetic hydrogen producing catalysts and provide both a template and an approach to measuring important physical properties of novel biomimetic candidates.

Conflicts of interest

There are no conflicts to declare.

Acknowledgements

We are grateful to Prof. Robin Perutz for valuable discussions. The work was funded by the Leverhulme Trust (RPG-2018-188). SLDW acknowledges PhD studentship funding from the University of York. Access to the STFC Central Laser Facility (20130007) is gratefully acknowledged. This work (Y. R. and M. H.) was funded by the DFG under Germany's Excellence Strategy—EXC 2008–390540038—UniSysCat.

References

1 W. Lubitz, H. Ogata, O. Rudiger and E. Reijerse, Hydrogenases, *Chem. Rev.*, 2014, **114**(8), 4081–4148.
2 M. J. Lukey, A. Parkin, M. M. Roessler, B. J. Murphy, J. Harmer, T. Palmer, F. Sargent and F. A. Armstrong, How Escherichia coli Is Equipped to Oxidize Hydrogen under Different Redox Conditions, *J. Biol. Chem.*, 2010, **285**(6), 3928–3938.
3 J. A. Birrell, O. Rudiger, E. J. Reijerse and W. Lubitz, Semisynthetic Hydrogenases Propel Biological Energy Research into a New Era, *Joule*, 2017, **1**(1), 61–76.
4 N. A. Eberhardt and H. R. Guan, Nickel Hydride Complexes, *Chem. Rev.*, 2016, **116**(15), 8373–8426.
5 P. W. Du and R. Eisenberg, Catalysts made of earth-abundant elements (Co, Ni, Fe) for water splitting: recent progress and future challenges, *Energy Environ. Sci.*, 2012, **5**(3), 6012–6021.
6 S. Fukuzumi, Y. M. Lee and W. Nam, Thermal and photocatalytic production of hydrogen with earth-abundant metal complexes, *Coord. Chem. Rev.*, 2018, **355**, 54–73.
7 T. Kramer, M. Kamp, W. Lubitz, M. van Gastel and F. Neese, Theoretical Spectroscopy of the Ni-II Intermediate States in the Catalytic Cycle and the Activation of NiFe Hydrogenases, *ChemBioChem*, 2013, **14**(14), 1898–1905.
8 M. Kampa, W. Lubitz, M. van Gastel and F. Neese, Computational study of the electronic structure and magnetic properties of the Ni-C state in NiFe hydrogenases including the second coordination sphere, *J. Biol. Inorg. Chem.*, 2012, **17**(8), 1269–1281.
9 Y. Ilina, C. Lorent, S. Katz, J. H. Jeoung, S. Shima, M. Horch, I. Zebger and H. Dobbek, X-ray Crystallography and Vibrational Spectroscopy Reveal the Key Determinants of Biocatalytic Dihydrogen Cycling by NiFe Hydrogenases, *Angew. Chem., Int. Ed.*, 2019, **58**(51), 18710–18714.
10 M. Bruschi, M. Tiberti, A. Guerra and L. De Gioia, Disclosure of Key Stereoelectronic Factors for Efficient H-2 Binding and Cleavage in the Active Site of NiFe-Hydrogenases, *J. Am. Chem. Soc.*, 2014, **136**(5), 1803–1814.
11 N. T. Nguyen, Y. Mori, T. Matsumoto, T. Yatabe, R. Kabe, H. Nakai, K. S. Yoon and S. Ogo, A NiFe hydrogenase model that catalyses the release of hydrogen from formic acid, *Chem. Commun.*, 2014, **50**(87), 13385–13387.
12 M. L. Helm, M. P. Stewart, R. M. Bullock, M. R. DuBois and D. L. DuBois, A Synthetic Nickel Electrocatalyst with a Turnover Frequency Above 100 000 $s^{(-1)}$ for H-2 Production, *Science*, 2011, **333**(6044), 863–866.
13 F. Wang, M. Wen, K. Feng, W. J. Liang, X. B. Li, B. Chen, C. H. Tung and L. Z. Wu, Amphiphilic polymeric micelles as microreactors: improving the photocatalytic hydrogen production of the FeFe-hydrogenase mimic in water, *Chem. Commun.*, 2016, **52**(3), 457–460.
14 L. Z. Wu, B. Chen, Z. J. Li and C. H. Tung, Enhancement of the Efficiency of Photocatalytic Reduction of Protons to Hydrogen via Molecular Assembly, *Acc. Chem. Res.*, 2014, **47**(7), 2177–2185.
15 T. R. Simmons, G. Berggren, M. Bacchi, M. Fontecave and V. Artero, Mimicking hydrogenases: from biomimetics to artificial enzymes, *Coord. Chem. Rev.*, 2014, **270**, 127–150.
16 J. X. Jian, Q. Liu, Z. J. Li, F. Wang, X. B. Li, C. B. Li, B. Liu, Q. Y. Meng, B. Chen, K. Feng, C. H. Tung and L. Z. Wu, Chitosan confinement enhances hydrogen photogeneration from a mimic of the diiron subsite of FeFe-hydrogenase, *Nat. Commun.*, 2013, **4**, 2695.
17 H. Y. Wang, W. G. Wang, G. Si, F. Wang, C. H. Tung and L. Z. Wu, Photocatalytic Hydrogen Evolution from Rhenium(I) Complexes to FeFe Hydrogenase Mimics in Aqueous SDS Micellar Systems: A Biomimetic Pathway, *Langmuir*, 2010, **26**(12), 9766–9771.

18 F. Gloaguen and T. B. Rauchfuss, Small molecule mimics of hydrogenases: hydrides and redox, *Chem. Soc. Rev.*, 2009, **38**(1), 100–108.
19 V. Firpo, J. M. Le, V. Pavone, A. Lombardi and K. L. Bren, Hydrogen evolution from water catalyzed by cobalt-mimochrome VI*a, a synthetic mini-protein, *Chem. Sci.*, 2018, **9**(45), 8582–8589.
20 S. R. Soltau, P. D. Dahlberg, J. Niklas, O. G. Poluektov, K. L. Mulfort and L. M. Utschig, Ru-protein-Co biohybrids designed for solar hydrogen production: understanding electron transfer pathways related to photocatalytic function, *Chem. Sci.*, 2016, **7**(12), 7068–7078.
21 I. Nath, J. Chakraborty and F. Verpoort, Metal organic frameworks mimicking natural enzymes: a structural and functional analogy, *Chem. Soc. Rev.*, 2016, **45**(15), 4127–4170.
22 B. Kandemir, L. Kubie, Y. X. Guo, B. Sheldon and K. L. Bren, Hydrogen Evolution from Water under Aerobic Conditions Catalyzed by a Cobalt ATCUN Metallopeptide, *Inorg. Chem.*, 2016, **55**(4), 1355–1357.
23 B. Kandemir, S. Chakraborty, Y. X. Guo and K. L. Bren, Semisynthetic and Biomolecular Hydrogen Evolution Catalysts, *Inorg. Chem.*, 2016, **55**(2), 467–477.
24 S. C. Silver, J. Niklas, P. W. Du, O. G. Poluektov, D. M. Tiede and L. M. Utschig, Protein Delivery of a Ni Catalyst to Photosystem I for Light-Driven Hydrogen Production, *J. Am. Chem. Soc.*, 2013, **135**(36), 13246–13249.
25 J. Esselborn, C. Lambertz, A. Adamska-Venkatesh, T. Simmons, G. Berggren, J. Nothl, J. Siebel, A. Hemschemeier, V. Artero, E. Reijerse, M. Fontecave, W. Lubitz and T. Happe, Spontaneous activation of FeFe-hydrogenases by an inorganic 2Fe active site mimic, *Nat. Chem. Biol.*, 2013, **9**(10), 607–609.
26 G. Berggren, A. Adamska, C. Lambertz, T. R. Simmons, J. Esselborn, M. Atta, S. Gambarelli, J. M. Mouesca, E. Reijerse, W. Lubitz, T. Happe, V. Artero and M. Fontecave, Biomimetic assembly and activation of FeFe-hydrogenases, *Nature*, 2013, **499**(7456), 66–69.
27 R. Hidalgo, P. A. Ash, A. J. Healy and K. A. Vincent, Infrared Spectroscopy During Electrocatalytic Turnover Reveals the Ni-L Active Site State During H-2 Oxidation by a NiFe Hydrogenase, *Angew. Chem., Int. Ed.*, 2015, **54**(24), 7110–7113.
28 A. L. De Lacey, V. M. Fernandez, M. Rousset and R. Cammack, Activation and inactivation of hydrogenase function and the catalytic cycle: spectroelectrochemical studies, *Chem. Rev.*, 2007, **107**(10), 4304–4330.
29 B. Bleijlevens, F. A. van Broekhuizen, A. L. De Lacey, W. Roseboom, V. M. Fernandez and S. P. J. Albracht, The activation of the NiFe-hydrogenase from Allochromatium vinosum. An infrared spectro-electrochemical study, *J. Biol. Inorg. Chem.*, 2004, **9**(6), 743–752.
30 M. Y. Darensbourg, E. J. Lyon and J. J. Smee, The bio-organometallic chemistry of active site iron in hydrogenases, *Coord. Chem. Rev.*, 2000, **206**, 533–561.
31 K. A. Bagley, E. C. Duin, W. Roseboom, S. P. J. Albracht and W. H. Woodruff, Infrared-detectable groups sense changes in charge-density on the nickel center in hydrogenase from Chromatium vinosum, *Biochemistry*, 1995, **34**(16), 5527–5535.
32 K. A. Bagley, C. J. Vangarderen, M. Chen, E. C. Duin, S. P. J. Albracht and W. H. Woodruff, Infrared studies on the interaction of carbon-monoxide with divalent nickel in hydrogenase from Chromatium-vinosum, *Biochemistry*, 1994, **33**(31), 9229–9236.
33 P. A. Ash, R. Hidalgo and K. A. Vincent, Proton Transfer in the Catalytic Cycle of NiFe Hydrogenases: insight from Vibrational Spectroscopy, *ACS Catal.*, 2017, **7**(4), 2471–2485.
34 S. Katz, J. Noth, M. Horch, H. S. Shafaat, T. Happe, P. Hildebrandt and I. Zebger, Vibrational spectroscopy reveals the initial steps of biological hydrogen evolution, *Chem. Sci.*, 2016, **7**(11), 6746–6752.
35 M. Horch, J. Schoknecht, M. A. Mroginski, O. Lenz, P. Hildebrandt and I. Zebger, Resonance Raman Spectroscopy on NiFe Hydrogenase Provides Structural Insights into Catalytic Intermediates and Reactions, *J. Am. Chem. Soc.*, 2014, **136**(28), 9870–9873.
36 E. Siebert, M. Horch, Y. Rippers, J. Fritsch, S. Frielingsdorf, O. Lenz, F. V. Escobar, F. Siebert, L. Paasche, U. Kuhlmann, F. Lendzian, M. A. Mroginski, I. Zebger and P. Hildebrandt, Resonance Raman Spectroscopy as a Tool to Monitor the Active Site of Hydrogenases, *Angew. Chem., Int. Ed.*, 2013, **52**(19), 5162–5165.
37 H. Ogata, T. Kramer, H. X. Wang, D. Schilter, V. Pelmenschikov, M. van Gastel, F. Neese, T. B. Rauchfuss, L. B. Gee, A. D. Scott, Y. Yoda, Y. Tanaka, W. Lubitz and S. P. Cramer, Hydride bridge in NiFe-hydrogenase observed by nuclear resonance vibrational spectroscopy, *Nat. Commun.*, 2015, **6**, 7890.
38 G. E. Vansuch, C. H. Wu, D. K. Haja, S. A. Blair, B. Chica, M. K. Johnson, M. W. W. Adams and R. B. Dyer, Metal-ligand cooperativity in the soluble hydrogenase-1 fromPyrococcus furiosus, *Chem. Sci.*, 2020, **11**(32), 8572–8581.
39 M. L. K. Sanchez, S. E. Konecny, S. M. Narehood, E. J. Reijerse, W. Lubitz, J. A. Birrell and R. B. Dyer, The Laser-Induced Potential Jump: A Method for Rapid Electron Injection into Oxidoreductase Enzymes, *J. Phys. Chem. B*, 2020, **124**(40), 8750–8760.
40 M. L. K. Sanchez, C. Sommer, E. Reijerse, J. A. Birrell, W. Lubitz and R. B. Dyer, Investigating the Kinetic Competency of CrHydA1 FeFe Hydrogenase Intermediate States via Time-Resolved Infrared Spectroscopy, *J. Am. Chem. Soc.*, 2019, **141**(40), 16064–16070.
41 B. L. Greene, G. E. Vansuch, B. C. Chica, M. W. W. Adams and R. B. Dyer, Applications of Photogating and Time Resolved Spectroscopy to Mechanistic Studies of Hydrogenases, *Acc. Chem. Res.*, 2017, **50**(11), 2718–2726.
42 B. L. Greene, G. J. Schut, M. W. W. Adams and R. B. Dyer, Pre-Steady-State Kinetics of Catalytic Intermediates of an FeFe-Hydrogenase, *ACS Catal.*, 2017, **7**(3), 2145–2150.
43 B. L. Greene, G. E. Vansuch, C. H. Wu, M. W. W. Adams and R. B. Dyer, Glutamate Gated Proton-Coupled Electron Transfer Activity of a NiFe-Hydrogenase, *J. Am. Chem. Soc.*, 2016, **138**(39), 13013–13021.

44 B. L. Greene, C. H. Wu, P. M. McTernan, M. W. W. Adams and R. B. Dyer, Proton-Coupled Electron Transfer Dynamics in the Catalytic Mechanism of a NiFe-Hydrogenase, *J. Am. Chem. Soc.*, 2015, **137**(13), 4558–4566.

45 B. L. Greene, C. A. Joseph, M. J. Maroney and R. B. Dyer, Direct Evidence of Active-Site Reduction and Photodriven Catalysis in Sensitized Hydrogenase Assemblies, *J. Am. Chem. Soc.*, 2012, **134**(27), 11108–11111.

46 N. T. Hunt, Transient 2D-IR spectroscopy of inorganic excited states, *Dalton Trans.*, 2014, **43**(47), 17578–17589.

47 N. T. Hunt, 2D-IR spectroscopy: ultrafast insights into biomolecule structure and function, *Chem. Soc. Rev.*, 2009, **38**(7), 1837–1848.

48 P. Hamm and M. T. Zanni, *Concepts and methods of 2D infrared spectroscopy*, Cambridge University Press, 2011.

49 M. Khalil, N. Demirdoven and A. Tokmakoff, Coherent 2D IR spectroscopy: molecular structure and dynamics in solution, *J. Phys. Chem. A*, 2003, **107**(27), 5258–5279.

50 M. C. Asplund, M. T. Zanni and R. M. Hochstrasser, Two-dimensional infrared spectroscopy of peptides by phase-controlled femtosecond vibrational photon echoes, *Proc. Natl. Acad. Sci. U. S. A.*, 2000, **97**(15), 8219–8224.

51 P. Hamm, M. H. Lim and R. M. Hochstrasser, Structure of the amide I band of peptides measured by femtosecond nonlinear-infrared spectroscopy, *J. Phys. Chem. B*, 1998, **102**(31), 6123–6138.

52 M. Horch, J. Schoknecht, S. L. D. Wrathall, G. M. Greetham, O. Lenz and N. T. Hunt, Understanding the structure and dynamics of hydrogenases by ultrafast and two-dimensional infrared spectroscopy, *Chem. Sci.*, 2019, **10**(39), 8981–8989.

53 H. Adamson, M. Robinson, J. J. Wright, L. A. Flanagan, J. Walton, D. Elton, D. J. Gavaghan, A. M. Bond, M. M. Roessler and A. Parkin, Retuning the Catalytic Bias and Overpotential of a NiFe-Hydrogenase via a Single Amino Acid Exchange at the Electron Entry/Exit Site, *J. Am. Chem. Soc.*, 2017, **139**(31), 10677–10686.

54 L. A. Flanagan, J. J. Wright, M. M. Roessler, J. W. Moir and A. Parkin, Re-engineering a NiFe hydrogenase to increase the H-2 production bias while maintaining native levels of O-2 tolerance, *Chem. Commun.*, 2016, **52**(58), 9133–9136.

55 A. L. DeLacey, V. M. Fernandez, M. Rousset, C. Cavazza and E. C. Hatchikian, Spectroscopic and kinetic characterization of active site mutants of Desulfovibrio fructosovorans Ni-Fe hydrogenase, *J. Biol. Inorg. Chem.*, 2003, **8**(1-2), 129–134.

56 G. M. Greetham, P. Burgos, Q. A. Cao, I. P. Clark, P. S. Codd, R. C. Farrow, M. W. George, M. Kogimtzis, P. Matousek, A. W. Parker, M. R. Pollard, D. A. Robinson, Z. J. Xin and M. Towrie, ULTRA: A Unique Instrument for Time-Resolved Spectroscopy, *Appl. Spectrosc.*, 2010, **64**(12), 1311–1319.

57 R. M. Evans, P. A. Ash, S. E. Beaton, E. J. Brooke, K. A. Vincent, S. B. Carr and F. A. Armstrong, Mechanistic Exploitation of a Self-Repairing, Blocked Proton Transfer Pathway in an O-2-Tolerant NiFe-Hydrogenase, *J. Am. Chem. Soc.*, 2018, **140**(32), 10208–10220.

58 S. F. A. Kettle, G. L. Aschero, E. Diana, R. Rossetti and P. L. Stanghellini, The vibrational spectra of the cyanide ligand revisited: terminal cyanides, *Inorg. Chem.*, 2006, **45**(13), 4928–4937.

59 K. G. V. Sigfridsson, N. Leidel, O. Sanganas, P. Chemev, O. Lenz, K. S. Yoon, H. Nishihara, A. Parkin, F. A. Armstrong, S. Dementin, M. Rousset, A. L. De Lacey and M. Haumann, Structural differences of oxidized iron-sulfur and nickel-iron cofactors in O-2-tolerant and O-2-sensitive hydrogenases studied by X-ray absorption spectroscopy, *Biochim. Biophys. Acta, Bioenerg.*, 2015, **1847**(2), 162–170.

60 A. Volbeda, C. Damault, A. Parkin, F. Sargent, F. A. Armstrong and J. C. Fontecilla-Camps, Crystal Structure of the O-2-Tolerant Membrane-Bound Hydrogenase 1 from Escherichia coli in Complex with Its Cognate Cytochrome *b*, *Structure*, 2013, **21**(1), 184–190.

61 K. A. Vincent, A. Parkin, O. Lenz, S. P. J. Albracht, J. C. Fontecilla-Camps, R. Cammack, B. Friedrich and F. A. Armstrong, Electrochemical definitions of O-2 sensitivity and oxidative inactivation in hydrogenases, *J. Am. Chem. Soc.*, 2005, **127**(51), 18179–18189.

62 S. Hume, G. Hithell, G. M. Greetham, P. M. Donaldson, M. Towrie, A. W. Parker, M. J. Baker and N. T. Hunt, Measuring proteins in H_2O with 2D-IR spectroscopy, *Chem. Sci.*, 2019, **10**(26), 6448–6456.

63 E. B. Dunkelberger, M. Grechko and M. T. Zanni, Transition Dipoles from 1D and 2D Infrared Spectroscopy Help Reveal the Secondary Structures of Proteins: Application to Amyloids, *J. Phys. Chem. B*, 2015, **119**(44), 14065–14075.

64 J. R. Zheng, K. Kwak, J. Asbury, X. Chen, I. R. Piletic and M. D. Fayer, Ultrafast dynamics of solute-solvent complexation observed at thermal equilibrium in real time, *Science*, 2005, **309**(5739), 1338–1343.

65 R. P. Happe, W. Roseboom, A. J. Pierik, S. P. J. Albracht and K. A. Bagley, Biological activation of hydrogen, *Nature*, 1997, **385**(6612), 126.

66 V. Cervetto, J. Helbing, J. Bredenbeck and P. Hamm, Double-resonance versus pulsed Fourier transform two-dimensional infrared spectroscopy: an experimental and theoretical comparison, *J. Chem. Phys.*, 2004, **121**(12), 5935–5942.

67 O. Golonzka, M. Khalil, N. Demirdoven and A. Tokmakoff, Coupling and orientation between anharmonic vibrations characterized with two-dimensional infrared vibrational echo spectroscopy, *J. Chem. Phys.*, 2001, **115**(23), 10814–10828.

68 C. H. Lai, W. Z. Lee, M. L. Miller, J. H. Reibenspies, D. J. Darensbourg and M. Y. Darensbourg, Responses of the Fe(CN)(2)(CO) unit to electronic changes as related to its role in NiFe hydrogenase, *J. Am. Chem. Soc.*, 1998, **120**(39), 10103–10114.

69 D. J. Darensbourg, J. H. Reibenspies, C. H. Lai, W. Z. Lee and M. Y. Darensbourg, Analysis of an organometallic iron site model for the heterodimetallic unit of NiFe hydrogenase, *J. Am. Chem. Soc.*, 1997, **119**(33), 7903–7904.

70 A. J. Pierik, W. Roseboom, R. P. Happe, K. A. Bagley and S. P. J. Albracht, Carbon monoxide and cyanide as intrinsic ligands to iron in the active site of NiFe-hydrogenases – NiFe(CN)(2)CO, biology's way to activate H-2, *J. Biol. Chem.*, 1999, **274**(6), 3331–3337.

71 M. H. Cho, Ultrafast vibrational spectroscopy in condensed phases, *Phys. Chem. Commun.*, 2002, **5**, 40–58.
72 K. Park, M. H. Cho, S. Hahn and D. Kim, Two-dimensional vibrational spectroscopy. II. Ab initio calculation of the coherent 2D infrared response function of $CHCl_3$ and comparison with the 2D Raman response function, *J. Chem. Phys.*, 1999, **111**(9), 4131–4139.
73 S. Hahn, K. Park and M. Cho, Two-dimensional vibrational spectroscopy. I. Theoretical calculation of the nonlinear Raman response function of $CHCl_3$, *J. Chem. Phys.*, 1999, **111**(9), 4121–4130.
74 S. Hahn, D. Kim and M. H. Cho, Nonlinear optical properties of the linear quadrupolar molecule: structure-function relationship based on a three-state model, *J. Phys. Chem. B*, 1999, **103**(39), 8221–8229.
75 K. M. Slenkamp, M. S. Lynch, B. E. Van Kuiken, J. F. Brookes, C. C. Bannan, S. L. Daifuku and M. Khalil, Investigating vibrational anharmonic couplings in cyanide-bridged transition metal mixed valence complexes using two-dimensional infrared spectroscopy, *J. Chem. Phys.*, 2014, **140**(8), 084505.
76 S. Kaziannis, J. A. Wright, M. Candelaresi, R. Kania, G. M. Greetham, A. W. Parker, C. J. Pickett and N. T. Hunt, The role of CN and CO ligands in the vibrational relaxation dynamics of model compounds of the FeFe-hydrogenase enzyme, *Phys. Chem. Chem. Phys.*, 2011, **13**(21), 10295–10305.
77 M. Horch, L. Lauterbach, M. A. Mroginski, P. Hildebrandt, O. Lenz and I. Zebger, Reversible Active Site Sulfoxygenation Can Explain the Oxygen Tolerance of a NAD(+)-Reducing NiFe Hydrogenase and Its Unusual Infrared Spectroscopic Properties, *J. Am. Chem. Soc.*, 2015, **137**(7), 2555–2564.
78 J. T. King, M. R. Ross and K. J. Kubarych, Water-Assisted Vibrational Relaxation of a Metal Carbonyl Complex Studied with Ultrafast 2D-IR, *J. Phys. Chem. B*, 2012, **116**(12), 3754–3759.
79 D. Weidinger, G. M. Sando and J. C. Owrutsky, Vibrational dynamics of metal cyanides, *Chem. Phys. Lett.*, 2010, **489**(4-6), 169–174.
80 D. Czurlok, J. Gleim, J. Lindner and P. Vohringer, Vibrational Energy Relaxation of Thiocyanate Ions in Liquid-to-Supercritical Light and Heavy Water. A Fermi's Golden Rule Analysis, *J. Phys. Chem. Lett.*, 2014, **5**(19), 3373–3379.
81 S. Park and M. D. Fayer, Hydrogen bond dynamics in aqueous NaBr solutions, *Proc. Natl. Acad. Sci. U. S. A.*, 2007, **104**(43), 16731–16738.
82 K. Adamczyk, N. Simpson, G. M. Greetham, A. Gumiero, M. A. Walsh, M. Towrie, A. W. Parker and N. T. Hunt, Ultrafast infrared spectroscopy reveals water-mediated coherent dynamics in an enzyme active site, *Chem. Sci.*, 2015, **6**(1), 505–516.
83 C. Ranasinghe, P. Pagano, P. J. Sapienza, A. L. Lee, A. Kohen and C. M. Cheatum, Isotopic Labeling of Formate Dehydrogenase Perturbs the Protein Dynamics, *J. Phys. Chem. B*, 2019, **123**(49), 10403–10409.
84 S. Ramos, R. E. Horness, J. A. Collins, D. Haak and M. C. Thielges, Site-specific 2D IR spectroscopy: a general approach for the characterization of protein dynamics with high spatial and temporal resolution, *Phys. Chem. Chem. Phys.*, 2019, **21**(2), 780–788.
85 P. Pagano, Q. Guo, C. Ranasinghe, E. Schroeder, K. Robben, F. Hase, H. P. Ye, K. Wickersham, A. Aspuru-Guzik, D. T. Major, L. Gakhar, A. Kohen and C. M. Cheatum, Oscillatory Active-Site Motions Correlate with Kinetic Isotope Effects in Formate Dehydrogenase, *ACS Catal.*, 2019, **9**(12), 11199–11206.
86 C. Ranasinghe, Q. Guo, P. J. Sapienza, A. L. Lee, D. M. Quinn, C. M. Cheatum and A. Kohen, Protein Mass Effects on Formate Dehydrogenase, *J. Am. Chem. Soc.*, 2017, **139**(48), 17405–17413.
87 H. Ishikawa, S. Kim, K. Kwak, K. Wakasugi and M. D. Fayer, Disulfide bond influence on protein structural dynamics probed with 2D-IR vibrational echo spectroscopy, *Proc. Natl. Acad. Sci. U. S. A.*, 2007, **104**(49), 19309–19314.
88 H. Ishikawa, I. J. Finkelstein, S. Kim, K. Kwak, J. K. Chung, K. Wakasugi, A. M. Massari and M. D. Fayer, Neuroglobin dynamics observed with ultrafast 2D-IR vibrational echo spectroscopy, *Proc. Natl. Acad. Sci. U. S. A.*, 2007, **104**(41), 16116–16121.
89 A. I. Stewart, I. P. Clark, M. Towrie, S. K. Ibrahim, A. W. Parker, C. J. Pickett and N. T. Hunt, Structure and vibrational dynamics of model compounds of the FeFe-hydrogenase enzyme system via ultrafast two-dimensional infrared spectroscopy, *J. Phys. Chem. B*, 2008, **112**(32), 10023–10032.
90 G. M. Bonner, A. R. Ridley, S. K. Ibrahim, C. J. Pickett and N. T. Hunt, Probing the effect of the solution environment on the vibrational dynamics of an enzyme model system with ultrafast 2D-IR spectroscopy, *Faraday Discuss.*, 2010, **145**, 429–442.
91 P. A. Ash, S. E. T. Kendall-Price, R. M. Evans, S. B. Carr, A. R. Brasnett, S. Morra, J. S. Rowbotham, R. Hidalgo, A. J. Healy, G. Cinque, M. D. Frogley, F. A. Armstrong and K. A. Vincent, The crystalline state as a dynamic system: IR microspectroscopy under electrochemical control for a NiFe hydrogenase, *Chem. Sci.*, 2021, **12**(39), 12959–12970.
92 H. L. Tai, L. Y. Xu, S. Inoue, K. Nishikawa, Y. Higuchi and S. Hirota, Photoactivation of the Ni-SIr state to the Ni-SIa state in NiFe hydrogenase: FT-IR study on the light reactivity of the ready Ni-SIr state and as-isolated enzyme revisited, *Phys. Chem. Chem. Phys.*, 2016, **18**(32), 22025–22030.
93 A. L. deLacey, E. C. Hatchikian, A. Volbeda, M. Frey, J. C. FontecillaCamps and V. M. Fernandez, Infrared spectroelectrochemical characterization of the NiFe hydrogenase of Desulfovibrio gigas, *J. Am. Chem. Soc.*, 1997, **119**(31), 7181–7189.
94 M. Saggu, I. Zebger, M. Ludwig, O. Lenz, B. Friedrich, P. Hildebrandt and F. Lendzian, Spectroscopic Insights into the Oxygen-tolerant Membrane-associated NiFe Hydrogenase of Ralstonia eutropha H16, *J. Biol. Chem.*, 2009, **284**(24), 16264–16276.

95 G. Caserta, C. Lorent, V. Pelmenschikov, J. Schoknecht, Y. Yoda, P. Hildebrandt, S. P. Cramer, I. Zebger and O. Lenz, In Vitro Assembly as a Tool to Investigate Catalytic Intermediates of NiFe-Hydrogenase, *ACS Catal.*, 2020, **10**(23), 13890–13894.
96 M. Horch, L. Lauterbach, M. Saggu, P. Hildebrandt, F. Lendzian, R. Bittl, O. Lenz and I. Zebger, Probing the Active Site of an O-2-Tolerant NAD(+)-Reducing NiFe-Hydrogenase from Ralstonia eutropha H16 by In Situ EPR and FTIR Spectroscopy, *Angew. Chem., Int. Ed.*, 2010, **49**(43), 8026–8029.
97 J. T. King, J. M. Anna and K. J. Kubarych, Solvent-hindered intramolecular vibrational redistribution, *Phys. Chem. Chem. Phys.*, 2011, **13**(13), 5579–5583.
98 J. T. King, C. R. Baiz and K. J. Kubarych, Solvent-Dependent Spectral Diffusion in a Hydrogen Bonded ''Vibrational Aggregate'', *J. Phys. Chem. A*, 2010, **114**(39), 10590–10604.